

Flexural rift flank uplift at the Rio Grande rift, New Mexico

C. David Brown and Roger J. Phillips

Department of Earth and Planetary Sciences, Washington University, Saint Louis, Missouri

Abstract. Like other Cenozoic continental rifts, the Rio Grande rift in Colorado and New Mexico exhibits prominent flanking uplifts. Several driving stresses and thermal-mechanical processes have been proposed to explain the origin of rift flank relief, which can be modeled to infer lithospheric structure. Although we have identified multiple uplift styles at the Rio Grande rift, only one range—the Sacramento Mountains—is attributable to flexural upwarping of the lithosphere, the process most suitable for geodynamic modeling and interpretation. We demonstrate that two common assumptions in such modeling potentially introduce serious errors. First, presuming only one mechanism acts to uplift the flanks is inappropriate; various forces influence flank topography at different depths and wavelengths and no single one is dominant. Second, the end-member boundary conditions of complete mechanical continuity or discontinuity (broken plate) at the range-bounding normal fault are, in general, not applicable at rift flanks. We examine alternative analytic plate flexure solutions by comparing them to finite element models of footwall flexure at a normal fault in a two-dimensional elastic plate undergoing extension. These simulations indicate that broken plate fits to rift flanks underestimate the plate thickness unless the uplift is large (at least ~1 km), which promotes decoupling between the hanging wall and footwall. If denudation dominates the flank unloading, as may commonly be the case, the best-fit broken plate thickness error can be even greater. Our flexural analysis of the Sacramento Mountains suggests that the Pecos River Valley originated as a flexural downwarp adjacent to the rift flank. Sensitivity tests of least-squares fits to the Sacramento Mountains imply typical plate thickness errors of <20%, although in extreme cases the combined errors may be ~50%. The average effective elastic lithosphere thickness is ~23 km. We find that elastic-plastic models of rift flank flexure are unable to provide meaningful constraints on the thermal structure of continental lithosphere.

1. Introduction

The Rio Grande rift (RGR) is one of the most thoroughly studied Cenozoic continental rifts, but it is perhaps the most complicated because of its superposition on other Cordilleran structures of the western United States. The rift extends over 1000 km from Colorado through New Mexico to Chihuahua, Mexico (Figure 1), and it shows substantial changes in basin and flank physiography along strike [Olsen *et al.*, 1987; Baldrige *et al.*, 1995]. The RGR has been the focus of numerous geologic and geophysical investigations, including seismic refraction, seismic reflection, teleseismic tomography, gravity, basin stratigraphy, heat flow, magmatism, xenolith geothermobarometry, and

apatite fission-track analyses. The large amount of data amassed on the RGR provides invaluable constraints on geodynamic models over a range of structural scales, from the upper crust to the entire lithosphere and upper asthenosphere.

In the present study we examine the lithosphere-scale flexural uplift of the rift flanks. Rift flank uplift has been attributed to a variety of mechanisms and driving forces. For instance, flank uplift has been explained with elastic, viscous, and elastic-viscous-plastic models of the lithosphere, and authors have invoked crustal thinning (i.e., basin formation) [Weissel and Karner, 1989], necking of the mechanical lithosphere [Chéry *et al.*, 1992], lateral heat conduction [Alvarez *et al.*, 1984], small-scale convection [Buck, 1986], erosion and denudation [Gilchrist and Summerfield, 1990], and dynamic flow stresses [Zuber and Parmentier, 1986] as responsible processes. Obviously, these mechanisms are not mutually exclusive; several are likely to contribute to flank uplift, and no one may dominate.

This paper is structured as follows. First, we discuss the flank uplifts at the Rio Grande rift and evaluate whether or not they originate by lithospheric flexure (section 2). We find that only one flanking range, the Sacramento Mountains in southeastern New Mexico, is convincingly flexural, and therefore only it can be modeled using flexural techniques. Second, we use the Sacramento Mountains to test existing flexural rift flank uplift models—specifically, whether common assumptions of a completely broken or continuous lithosphere are reasonable, and whether a basin load can fully account for the uplift (section 3). We employ finite element models to investigate the role of an explicit, range-bounding normal fault on the behavior of the lithosphere (section 4). With the results of these simulations, we determine the effective elastic thickness of the lithosphere at the Sacramento Mountains as well as the uncertainty in this value (section 5). We end with a discussion of the relevance of our results to flexural rift flank modeling and the tectonics of southeastern New Mexico (section 6).

All of our modeling assumes an elastic lithosphere. An eventual goal, to which this work contributes, is to determine if flexural methods can be used as probes of the thermal structure of rifted continental lithosphere (as has been done with oceanic lithosphere [McNutt, 1984; Wessel, 1992]), or, conversely, if independent information on the geotherm can be used to test the mechanical and rheological precepts of lithospheric deformation modeling.

2. Flank Uplifts at the Rio Grande Rift

2.1. Background

Extension at the Rio Grande rift was preceded by several key geologic events that significantly influenced the late-Cenozoic rifting phase, including the flank structures. Two orogenies modified the crust of the North American craton where the RGR later formed: the Ancestral Rocky Mountains in the late Paleozoic

Copyright 1999 by the American Geophysical Union.

Paper number 1999TC900031.
0278-7407/99/1999TC900031\$12.00

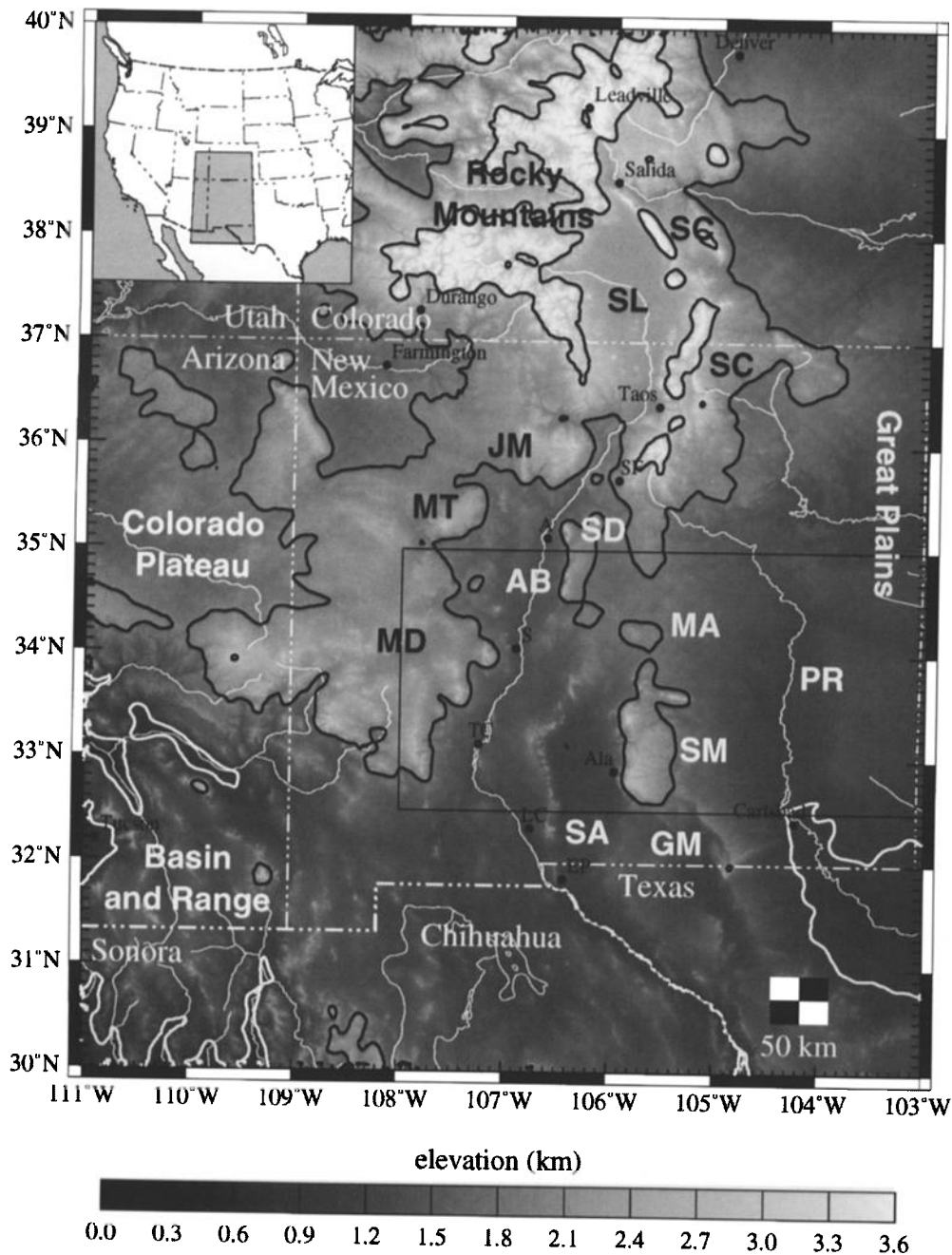


Figure 1. Topography and rivers of the Rio Grande rift region in Colorado, New Mexico, Texas, and northern Mexico. Long-wavelength topography is contoured at 1-km intervals (the white contour is 1-km elevation). Abbreviated major cities (north to south) are SF—Santa Fe, A—Albuquerque, S—Socorro, TC—Truth or Consequences, Ala—Alamosa, LC—Las Cruces, and EP—El Paso. Major features include SC—Sangre de Cristo Mountains, SL—San Luis Basin, JM—Jemez Mountains, MT—Mount Taylor, SD—Sandia Mountains, AB—Albuquerque Basin, MA—Mescalero arch, MD—Mogollon-Datil volcanic field, PR—Pecos River, SM—Sacramento Mountains, SA—San Andres Mountains, and GM—Guadalupe Mountains. Location of Figure 2a is outlined by box.

(~300 Ma) and the Laramide orogeny in the Late Cretaceous to early Tertiary (~80–40 Ma) [Chapin and Seager, 1975; Burchfiel *et al.*, 1992]. Topography was beveled during and following the Laramide, forming the low-relief Eocene erosion surface [Epis and Chapin, 1975; Gregory and Chase, 1994]. In the middle Tertiary (~40–20 Ma), voluminous intermediate-rhyolitic mag-

matism related to subduction of the Farallon plate emplaced large volcanic fields such as the Mogollon-Datil [e.g., Keller *et al.*, 1991; Baldrige *et al.*, 1995]. Initiation of extension in the late Oligocene (~29–27 Ma) is marked by a change in magmatic style to basaltic and bimodal, deposition of ash-flow tuffs, and development of early rift structures [Ingersoll *et al.*, 1990; Brister and

Gries, 1994; Chapin and Cather, 1994]. Two phases of extension and volcanism are commonly described for the rift [Morgan *et al.*, 1986]. The first was characterized by broad basins and low-angle normal faulting; it overlapped the end of the mid-Tertiary magmatic episode. The lithosphere is inferred to have been hot and weak; topographic relief generated during this phase was apparently modest. The second period of extension formed the primary features of the RGR we see today. High-angle normal faults accommodated strains of ~10–30%. Volcanism was less voluminous during this time.

2.2. Types of Flank Uplifts

The RGR is flanked by topographic highs along most of its length (Figure 1), but the nature and origin of these uplifts varies along rift strike. Flank topography is associated with Laramide basement-cored uplifts (which might have experienced additional, later uplift during rifting), volcanic structures, tilted fault blocks, and flexural uplifts. These features are all superimposed upon a regional, long-wavelength (>500-km) topographic upwarp [Eaton, 1987] that may have arisen from Laramide crustal thickening [Chapin and Cather, 1994], a remnant thermal anomaly from arc volcanism associated with subduction of the Farallon plate [Davis, 1991], prerift or synrift magmatic crustal thickening [Morgan *et al.*, 1986], or rift-driven asthenospheric upwelling [Bridwell and Anderson, 1980].

Several large volcanic fields along the western margin of the rift interfere with identification of possible tectonic uplift. Prominent examples include the Jemez Mountains (JM), the Mount Taylor volcanic shield (MT), and the Mogollon–Datil volcanic field (MD in Figure 1). The latter, though it is bordered by several rises on the east (Magdalena Mountains, San Mateo Mountains, and Black Ranges), has a deformation history dominated by volcanic processes, such as caldera formation and collapse [Coney, 1976]. It is difficult to distinguish tectonic uplift from these structures, making geodynamic modeling problematical.

2.3. Northern Rio Grande Rift

The northern and central RGR (north of Socorro, New Mexico, at 34°N) is narrow, and the rift is bounded to the west by the Colorado Plateau and to the east by the Great Plains (i.e., the North American craton). Rift basins are no more than 100 km wide. Here the flanks are delineated by prominent exposures of Proterozoic basement that stand out from the surrounding Phanerozoic sedimentary strata and Neogene rift-basin infill [Woodward *et al.*, 1975; Baldrige *et al.*, 1983]. Some of these ranges are continuous, ~100-km-long features (e.g., Sangre de Cristo Mountains (SC), Los Pinos–Manzano–Sandia Mountains (SD in Figure 1)) while others are isolated blocks bounded on two or three sides by normal faults (e.g., Lemitar Mountains, Ladron Peak [May *et al.*, 1994]). The southern Rocky Mountains were uplifted during the Laramide orogeny, but some ranges experienced further uplift during late Tertiary rifting [Tweto, 1975]. For example, the Sangre de Cristo Mountains in south-central Colorado comprise the eastern edge of a broader Laramide uplift, part of which was down-faulted as the San Luis Basin graben (SL in Figure 1). The Sangre de Cristo Mountains are now bordered on both the west and east by Neogene normal

faults that express additional uplift during rifting [Tweto, 1979]. Similarly, the Los Pinos–Manzano uplift is a composite of Laramide and Rio Grande uplifts [Kelley, 1979].

Kelley and Duncan [1986] and Kelley *et al.* [1992] performed detailed apatite fission track (AFT) analyses of rocks from several northern and central RGR flanks. AFT dates reflect the time since the rock rose through the $100 \pm 40^\circ\text{C}$ isotherm, as fission tracks anneal at higher temperatures. However, hydrothermal processes and magmatism can mimic the effects of denudation-induced uplift and cooling. Kelley *et al.* [1992] found AFT ages indicative of Laramide deformation, late Eocene denudation, rift-related uplift, and volcanic and hydrothermal modification. The former two processes involved slow cooling rates ($<5 \text{ K Myr}^{-1}$) and show AFT ages greater than 30 Ma. Uplifts attributed to rifting, but spared the effects of volcanism, have AFT ages of 10–25 Ma and include the northern Sangre de Cristo Mountains, Blanca Peak, the Sandia Mountains, and Ladron Peak. These rocks experienced relatively rapid cooling rates of $>5 \text{ K Myr}^{-1}$ and ascended at least 2–3 km.

The AFT results demonstrate that several flanks did form by uplift during rifting, including ranges that were first uplifted as Laramide basement-cored anticlines. There is a clear correlation between the locations of major rift-bounding normal faults and flanks exhibiting significant Neogene uplift [May *et al.*, 1994]. For instance, the Albuquerque Basin (AB in Figure 1) is the deepest half-graben of the rift (with over 7 km of synrift sediments [Russell and Snelson, 1994]); the adjacent Sandia Mountains have some of the highest Precambrian basement structural relief of the rift (over 3 km [Woodward *et al.*, 1975]), and among the fastest cooling rates (up to 12 K Myr^{-1} [Kelley *et al.*, 1992]). These observations imply that faulting and thinning of the crust drive rift flank uplift by unloading of the footwall.

2.4. Southern Rio Grande Rift

The southern RGR (south of Socorro) is distinct in character from the north: the rift widens and physiographically resembles the Basin and Range, into which it merges south of the Colorado Plateau (Figure 1). The flanks are dominated by ranges in the Mogollon–Datil volcanic field (MD) on the west and the Sacramento Mountains (SM) on the east. The interior is divided into several sub-basins (Palomas, Jornada del Muerto, and Tularosa) and structural highs such as the San Andres Mountains (SA in Figure 1). The flanks are composed of Tertiary volcanic and Paleozoic sedimentary rocks but not Precambrian basement [Woodward *et al.*, 1975; Baldrige *et al.*, 1983]. Like the central RGR, here the flanks are generally narrower and not as long as in the north. Southern basins are not as deep [Lozinsky, 1987; Harrison, 1994; Adams and Keller, 1994], but late-phase extension was apparently greater than in the north because the crust at the rift axis is thinner [Cordell, 1982; Morgan *et al.*, 1986].

AFT analyses indicate Miocene uplift ages for interior fault blocks of the southern rift, like the Caballo and San Andres Mountains [Kelley and Chapin, 1997]. There is essentially no Laramide AFT signature in the southern RGR, suggesting the net Laramide and late-Tertiary uplift is less compared to the north. AFT dating of two Proterozoic metasedimentary samples at the base of the western scarp of the Sacramento Mountains yielded ages of 35–41 Ma. Combined with age and apatite fission track

length measurements of samples at higher elevations, these results reflect a fairly slow uplift synchronous with late rifting [Kelley and Chapin, 1997].

2.5. Implications for Modeling

From the preceding overview of Rio Grande rift flank uplifts we can begin to explore the likely tectonic uplift mechanisms and determine if any flanks involve flexure of the lithosphere. Flank topography north of Santa Fe is dominantly Laramide in origin. Eocene denudation and rift-related unloading have contributed to uplift, as demonstrated by AFT dating, but preexisting orogenic topography and structural complexity preclude any straightforward mechanical interpretation of RGR uplift. These ranges lack cross-sectional topographic asymmetry diagnostic of flexural flank uplift. Although several uplifts in the central rift (between Socorro and Santa Fe) are directly attributable to rifting by their more modest Laramide deformation, AFT ages, and association with late-Tertiary normal faults and deep half grabens, they, too, are quite structurally complicated.

For example, the Sandia Mountains appear to represent a "classic" rift flank uplift. This range comprises an eastward-tilted fault block on the eastern margin of the Albuquerque Basin. Uplift was accommodated by one or more west-dipping normal faults [Kelley and Northrop, 1975]; net structural relief across these range-bounding faults exceeds 10 km [Chapin and Cather, 1994]. Laramide faults are evident, and the Sandia Mountains may have been the site of a Laramide anticline. The ~20-km-long range is bordered to the south by a northeast-striking Laramide fault, and to the north by a northeast-striking normal fault. The back slope of the mountains is thoroughly cut by faults that have experienced both reverse and normal motions, some of which may have been concurrent with late Tertiary uplift [Kelley and Northrop, 1975]. Other flanking ranges similar in both scale and structure to the Sandia Mountains include Ladron Peak and the Sierra Lucero [Lewis and Baldrige, 1994]; these mountains all experienced late Tertiary uplift, are of the order of 10 km in planform scale, and are bounded on two or more sides by faults. Extensional unloading of these three fault blocks certainly was a cause of their uplift, but they lack structural continuity parallel to the rift strike and the crust lacks mechanical continuity due to pervasive faulting (perhaps relict Laramide deformation). The first factor makes a two-dimensional modeling approximation inappropriate, and any three-dimensional model would require inclusion of the multiple controlling faults. Furthermore, deformation of these fault blocks probably contains no information on the lithospheric thickness or geotherm. We do not pursue modeling of these uplifts.

2.6. Sacramento Mountains

Only one range at the RGR, the Sacramento Mountains (SM), is a compelling example of a flexural rift flank uplift. This ~60-km-long, ~1.5-km-high range defines the eastern boundary of the RGR with the Great Plains (Figures 1 and 2), and it is bordered to the west by the Tularosa Basin (TB) and to the east by the Pecos River Valley (PR). While not as well studied as many regions in the central and northern rift, some limited but thorough field work in the TB-SM area substantiates the interpretation of a flank uplift at the SM concurrent with rifting. Pray [1961] mapped the SM, focusing on the thick Paleozoic sedimentary

section exposed in the dramatic west-facing escarpment. He observed that most structures in the area trend north and date to the Pennsylvanian-Permian (Ancestral Rocky Mountains) [Bowsher, 1991]. This was a period of uplift of what is called the Pedernal Mountains [e.g., Kelley, 1971]. The nearly complete absence of Mesozoic rocks in the area reflects substantial erosion at least into the early Cenozoic and the formation of the Sacramento Mountains peneplain [Kelley, 1971]. Structurally there is little evidence for significant Laramide deformation at the SM, and Kelley and Chapin's [1997] AFT age measurements lack a strong signature of Laramide uplift. Minor Tertiary volcanism in the SM is expressed by sills and dikes crossing the range [Pray, 1961], although the more substantial Sierra Blanca igneous complex and Capitan pluton are situated to the north [Moore et al., 1991].

The present form of the SM results from late Cenozoic uplift accommodated by slip on one or more major west-dipping normal faults at the eastern edge of the Tularosa Basin. These motions resulted in a north-trending topographically asymmetric mountain range with a steep west-facing escarpment and the gentle east-dipping Pecos slope [Bartsch-Winkler, 1995] (Figure 2b). The youth of the uplift is demonstrated by the truncation of the peneplain and volcanic intrusives by the escarpment [Pray, 1961], the ~40-Ma AFT ages from two Proterozoic samples near the base of the escarpment [Kelley and Chapin, 1997], the predominantly Neogene-aged sediments infilling the adjacent Tularosa Basin [Lozinsky and Bauer, 1991], and Quaternary and Holocene fault scarps along the TB margin [Machette, 1987]. Minimum stratigraphic offsets on the central segment of the uplift are 2000 m [Pray, 1961].

Unlike the broad Laramide ranges in the northern RGR, the Sacramento Mountains were dominantly uplifted in the late Tertiary and display an asymmetric profile. Erosion apparently beveled preexisting Paleozoic and any Laramide relief, leaving a relatively level surface prior to rifting. Also distinct from the small, narrow fault blocks of the central and southern rift, the SM are a major, continuous structure. They are bounded by faulting on only one edge and are not cut by late Tertiary faults on the back slope. Free air gravity is highly correlated with the SM topography, and a strong isostatic residual gravity anomaly over the SM [Heywood, 1992] is indicative of upward lithospheric flexure [Kooi et al., 1992]. We interpret the above evidence to show that the SM represent a flexural deformation of the lithosphere in response to driving forces associated with opening of the RGR. The SM are therefore a suitable subject for flexural modeling.

2.7. Pecos River Valley

The development of the Pecos River Valley (PR) is intimately related to the uplift of the SM (Figure 1). The Pecos River did not exist before the late Pliocene; drainages from the Southern Rocky Mountains flowed southeast across the present Southern High Plains (Llano Estacado) for most of the Tertiary. This was a period of moist climate and active erosion. In the late Miocene, changes related to topographic uplift at the RGR and a transition to a more semiarid climate resulted in deposition of Ogallala Formation sands and gravels on the Great Plains [Walker, 1978; Frye et al., 1982; Gustavson et al., 1990]. The oldest dated Ogallala strata are ~11 Ma [Winkler, 1987; Caran, 1991].

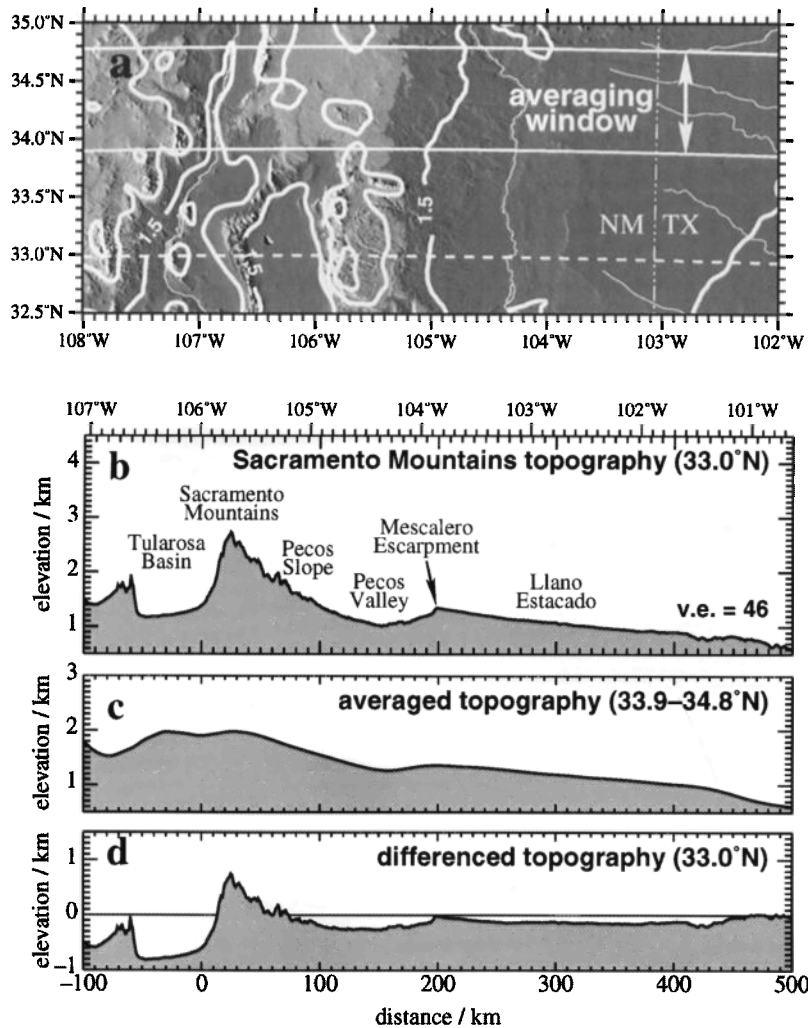


Figure 2. Separation of short- and long-wavelength topography at the Sacramento Mountains. (a) Elevations contoured in 500-m intervals over a shaded relief rendition of topography (cf. Figure 1). Areas with elevations above 1.8 km have a lighter shade, marking the broad north-trending eastern flank of the Rio Grande rift—the Mescalero arch and Sacramento Mountains. Window of averaged east–west profiles is indicated, as is the trace of the 33°N profile. (b) Original topography at 33°N. (c) Averaged and smoothed Mescalero arch east–west cross section. (d) Differenced topography: original elevations minus averaged cross section. Vertically exaggerated (v.e.) by a factor of 46.

Fluvial Ogallala deposits were mostly replaced by eolian materials at ~ 7 Ma [Gustavson *et al.*, 1990; Caran, 1991]. This change also reflects a drier climate, but it is primarily attributable to diversion of the southeast-flowing streams on the High Plains by the south-flowing Pecos River. An ancestral Pecos drainage in northwest Texas may have existed earlier in the Miocene, but Ogallala outcrops west of the present Pecos River as far south as 32°N [Frye *et al.*, 1982] seemingly preclude a major drainage in southeast New Mexico at that time. By the late Pliocene, the Pecos River existed east of the SM, and by the Pleistocene it had eroded headward to the Sangre de Cristo Mountains [Bachman, 1976]. Another view holds that the Pecos River developed to the south rather than by headward erosion [Gustavson and Finley, 1985].

The formation of the Pecos Valley probably postdated deposition of the fluvial Ogallala sediments, assuming that they were

transported across a continuous, relatively planar surface from their source areas in the west [Frye *et al.*, 1982]. However, eolian deposition of the upper Ogallala would not have been impeded by the presence of the valley, which in fact was an important source for these sediments. Hence an incipient Pecos River Valley probably existed in the late Miocene. Development of this valley is commonly ascribed to two processes: fluvial erosion and collapse caused by groundwater dissolution of Permian evaporite beds [e.g., Gustavson and Finley, 1985; McGookey *et al.*, 1988]. A possible difficulty with salt dissolution is that salt beds are absent beneath the Pecos slope even though it has not subsided. If the Permian evaporites tapered out to the west at the current location of the Pecos Valley, dissolution would have been responsible for much less subsidence. We suggest that a third mechanism—flexural downwarping—caused Pecos River Valley subsidence, and may have nucleated aqueous processes. This argument is based

on the spatial association of the valley peripheral and parallel to the SM and our flexural fits (section 5). There is also an inferred temporal association as the SM were a source for Ogallala clasts and must have had some relief by ~11 Ma. Initial uplift of the Guadalupe Mountains to the south (GM in Figure 1), which have a similar origin and geometry to the SM, has been dated at 11 Ma [Polyak *et al.*, 1998].

3. Broken and Continuous Elastic Plate Flexure

In this and the following sections we apply three types of two-dimensional lithospheric flexure models to the Sacramento Mountains with the purpose of determining the best approach to analyzing rift flank flexure. We begin with the simplest analytic elastic-plate models that have a specified line-load boundary condition. We follow with somewhat more sophisticated models that tie the mechanical response of the rifted lithosphere to the distributed loads at the surface and at depth. Next we compare analytic models to finite element models that explicitly include a fault within the plate (section 4). Finally, we derive an effective elastic thickness for the SM using the results of these comparisons (section 5).

3.1. Line-Load Models

The most direct approach to modeling flexure is to assume an entirely elastic plate and to specify (or solve for) boundary conditions at the origin [Zandt and Owens, 1980]. A plane-strain solution for the vertical displacements (w) as a function of distance (x) of a thin elastic plate in mechanical equilibrium with an applied line load is [Turcotte and Schubert, 1982, ch. 3]

$$w(x) = \left[A \sin\left(\frac{x}{\lambda}\right) + B \cos\left(\frac{x}{\lambda}\right) \right] \exp\left(-\frac{x}{\lambda}\right) \quad (1)$$

We label this the "general solution." The flexural wavelength (or parameter) is defined as

$$\lambda = \left(\frac{4D}{\rho g} \right)^{1/4} \quad (2)$$

and the flexural rigidity is

$$D = \frac{Eh_e^3}{12(1-\nu^2)} \quad (3)$$

The density ρ refers to the inviscid substrate beneath the plate; g is gravitational acceleration, E is Young's modulus, ν is Poisson's ratio, and h_e is the elastic plate thickness.

The vertical shear force (per unit length) at the origin, equivalent to the applied line load (positive up) is given by

$$V_0 = \frac{2D}{\lambda^3}(A+B) \quad (4)$$

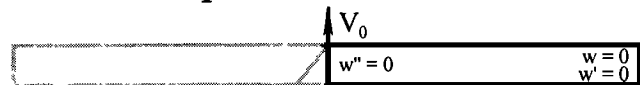
For a broken plate the bending curvature, moment, and stress are zero at the origin (Figure 3a), giving $A = 0$. For a continuous plate the slope is zero at the origin (Figure 3b) which requires $A = B$. The flexural bulge of the hanging wall is implicitly downfaulted so that the net displacements result in a basin.

We define the origin for the SM modeling with a linear approximation to the surface trace of the bounding normal fault.

The fault trace in the Tularosa Basin is sinuous, but it has an azimuth of N15°W as mapped by Pray [1961] and Woodward *et al.* [1975]. The lithospheric thickness and applied load inferred from matching flexural solutions to flank topography are sensitive to the location of this origin. We recognize a further uncertainty due to the dip of the fault; that is, it is unclear what depth along the fault plane should be used to define the horizontal origin. The accommodation of uplift on multiple faults introduces additional uncertainties. We use east-trending topographic cross sections for model fitting because the elevation contours on the Pecos Slope trend north (Figure 2a).

A least-squares fit of the broken plate model to the SM profile using the parameters of Table 1 gives a best-fit elastic plate thickness of 42 km. Alternatively, fitting the continuous plate model with the line load at the origin yields a 25-km elastic plate.

a. broken plate



flexural response



b. continuous plate



flexural response



kinematic response



total displacements



Figure 3. Broken and continuous elastic plate flexure. (a) For a broken plate, footwall uplift is assumed to be mechanically independent of the hanging wall. The boundary condition is zero bending curvature (moment) at the fault, and a vertical force (V_0) represents the unloading at this edge. (b) If the plate is continuous, the applied force or distributed stresses cause upwarping of the lithosphere. The superimposed effect of fault slip and basin subsidence results in an asymmetric flank-basin system.

Table 1. Physical Constants

Parameter	Definition	Value
E	Young's modulus	65 GPa
g	gravity at surface	9.80 m s^{-2}
ρ_s	sediment infill density	2100 kg m^{-3}
ρ_c	crustal density	2800 kg m^{-3}
ν	Poisson's ratio	0.25

A continuous plate might be dominantly loaded at the rift axis rather than at the flanks; shifting the origin to the west can give a 45-km-thick elastic plate. Therefore, changes in the type and location of the flank-uplift boundary condition can produce a range of elastic thickness estimates approaching a factor of 2. So far we have neglected to address many additional free parameters in the analysis and clearly the above flexural results are extremely nonunique. A possible solution to the boundary condition dilemma is to constrain the loads acting on the lithosphere from geologic information and not treat the load as a free parameter. Given independent information on the loading mechanisms, positions, and magnitudes (e.g., Tularosa Basin dimensions and infill density), we can limit our boundary condition choices and perhaps better determine the lithospheric thickness.

3.2. Residual Flank Topography

Before pursuing flexure models with prescribed distributed loads, we concern ourselves with the variety of processes responsible for topography at the SM. We wish to isolate the relief produced by shallow loads like basin infill and flank erosion that are compensated by lithospheric flexural rigidity. We note that a wide topographic rise, the Mescalero arch (distinct from the Mescalero escarpment), trends north of the SM along the eastern rift flank at $\sim 105.5^\circ\text{W}$ (MA in Figure 1, Figure 2a). This uplift is not bordered by major normal faults or basins [Woodward *et al.*, 1975], unlike the SM. It may have originated before rifting, perhaps during the Laramide orogeny [Kelley, 1971], or it may reflect a deep density anomaly of uplifted hot asthenosphere beneath the RGR [e.g., Slack *et al.*, 1996] related to lithospheric necking. This broad, deeply compensated uplift is of regional extent, and it probably also accounts for some of the SM relief. A long-wavelength topographic uplift that cannot be flexurally supported is also present in the Cordillera and Great Plains [Eaton, 1987]. We might simulate these components of the SM uplift by estimating the deep loads from seismic velocities and gravity (which reflect thermal and density anomalies) [Parker *et al.*, 1984] and applying them to our flexure models. However, there are substantial uncertainties involved in determining the magnitude and distribution of stresses from these data.

Instead, we separate the short-wavelength flexural topography attributed to shallow unloading (e.g., faulting, basins, and erosion) from the long-wavelength uplift associated with deep thermal and compositional buoyancy loads. We perform this separation by averaging 100 east-west topographic profiles over the unfaulted Mescalero arch ($33.9\text{--}34.8^\circ\text{N}$), which we assume has no short-wavelength flexural component, and subtracting this averaged profile from the SM cross sections (Figure 2). This manipulation is strictly valid only if the deep-seated loads and the

flexural rigidity are the same at the SM and the Mescalero arch, a reasonable supposition given the $\sim 150\text{-km}$ north-south distance of these two features. The residual topography has a much smaller SM flank amplitude, less than 1 km (Figure 2d), which is presumably independent of all deep loads. We fit the succeeding models to these short-wavelength topographic profiles.

3.3. Distributed-Load Models

Several workers have taken the approach of applying a known or inferred distributed load to a continuous elastic plate in performing rift flank flexure modeling [e.g., Weissel and Karner, 1989; Egan, 1992]. One can designate a fault geometry (planar or listric, dip, and décollement depth), apply a heave to the hanging wall, and thereby calculate the horizontal distribution of upward-directed reduced overburden stress on the lithosphere (for a particular choice of infill, crust, and mantle densities). Other loads may be included in this analysis, such as replacement of crust by mantle due to pure shear thinning of the lower crust (a downward stress), reduction in density due to uplifted isotherms and thermal expansion (an upward stress), and erosion of positive topography (an upward stress). The net laterally distributed stresses are included in the forward solution of the flexure equation for a continuous elastic plate. The flexural displacements are superimposed on those arising from slip on the fault (Figure 3b); therefore, this approach assumes a kinematic description of the extension, and it treats separately the mechanical response of the lithosphere to this extension.

We implement a variation on this technique for the Sacramento Mountains. We solve the flexure equation for an elastic plate subject to a distributed load using a finite difference method [Mueller and Phillips, 1995]. The structure of the Tularosa Basin is complex, and it is not satisfactorily described by a normal fault only at the eastern edge [Lozinsky and Bauer, 1991; Adams and Keller, 1994]. The basin has also been down-dropped at the western edge, adjacent to the San Andres Mountains, and encloses a buried north-trending horst. To test the continuous plate, distributed-load model, we define a simplified polygonal basin designed to maximize the unloading stresses. The model basin is 60 km wide, 2 km deep, and bounded by 60° faults; the crustal density is 2800 kg m^{-3} and the infill density is 2100 kg m^{-3} (Figure 4a). (Measured densities of Santa Fe Group sediments in the San Luis basin are $1900\text{--}2600 \text{ kg m}^{-3}$ [Keller *et al.*, 1984], with a depth-weighted mean of 2200 kg m^{-3} .) These parameter choices should maximize the vertical unloading stress, which attains 14 MPa (Figure 4a). For comparison, we show the contribution of pure shear (mantle uplift and thermal expansion) to buoyancy stresses assuming a sinusoidal variation in extension centered over the basin, with the net extension equal to the 2.3-km total heave on the faults. Parameter values are similar to those of Weissel and Karner [1989]. Pure shear contributes a negligible stress compared to the basin (dotted line, Figure 4a). The stress caused by thinning the crust and forming the basin, which integrates to a force of $8 \times 10^{11} \text{ N m}^{-1}$, results in only a few hundred meters of flexural uplift, even for a thin lithosphere; the modeled flank relief is almost a factor of 10 smaller than the SM residual topography (Figure 4b). This result implies that we have left out important loads and/or that the continuous plate assumption is not applicable.

Another significant applied stress is produced by denudation of the footwall fault scarp. Eroded material is transferred into the

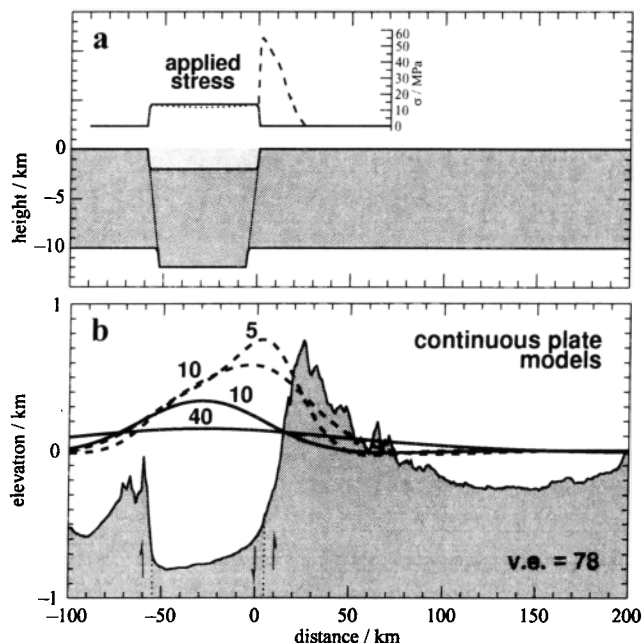


Figure 4. Continuous plate model of rift-flank flexure for a specified stress distribution. (a) Lower cross section shows assumed Tularosa Basin geometry. Applied stresses resulting from the replacement of crust by basin infill (solid line), the basin plus pure shear in the lithosphere (dotted line), and the basin plus erosion on the flank (dashed line) are plotted in the upper diagram. (b) Sacramento Mountains residual topography at 33°N. Solid curves are continuous plate flexural solutions for the basin infill load alone, with elastic plate thicknesses of 10 and 40 km. Dashed curves are continuous plate solutions for combined basin infill and erosional loads, with elastic plate thicknesses of 5 and 10 km. Normal faults are drawn at their mapped locations.

basin and the removed mass causes a substantial upward load. We estimate the stress distribution due to erosional unloading by calculating the cross-sectional area of missing rock between the fault and the crest of the SM. We assume a 60° dip to the master fault and extrapolate the Pecos slope to the west with a 2° dip. We assign a density of 2800 kg m⁻³ to the eroded crust. This stress distribution is plotted with the dashed line in Figure 4a. The horizontally integrated erosional force is 7×10^{11} N m⁻¹, comparable to the basin infill load. Varying the fault dip by $\pm 15^\circ$ causes a negligible (<3%) change in this force. Figure 4b shows continuous plate flexural deflection curves for 5- and 10-km elastic plates subject to the combined basin and erosion loads; these solutions are still unable to match either the amplitude or shape of the SM. The continuous plate condition forces the uplift to occur too far west; a thicker lithosphere distributes the uplift farther east, but then produces too small an amplitude. A lower datum (e.g., the base of the Pecos Valley) would produce even greater misfits.

Denudation of the Pecos slope may also have contributed to unloading of the SM. Late Tertiary erosion of this surface has undoubtedly occurred because the eastern flanks of the RGR were one source of the Ogallala Formation on the Great Plains. Examination of geologic cross sections published by *Bartsch-Winkler* [1995] and *McGookey et al.* [1988] suggests the degree of erosion is similar to that on the Mescalero arch; thus, to first

order, the isostatic effects of such erosion have been removed from the residual topography (Figure 2). The continuous plate model will match the SM residual topography with an additional ~20-MPa peak stress that decreases linearly to the east across the Pecos slope. This load corresponds to an additional 700 m of denudation at the crest, exceeding plausible amounts of differential erosion between the SM and Mescalero arch as well as between the SM and Pecos River. We conclude that the continuous plate flexural model is not viable at the SM—provided that we have fully accounted for all loads, a caveat we return to in section 6.3. We must consider at least partial decoupling at the range-bounding fault.

4. Finite Element Models Including a Fault

Given the apparent shortcomings of the continuous plate model, we must also ask if the broken plate solution is an appropriate representation of footwall flexure. To address this question we take the approach of using finite element modeling (FEM) of flank uplift associated with normal faulting of an elastic lithosphere to test whether the broken plate equation fit to FEM solutions accurately determines the plate thickness. This approach is founded on two premises. First, we assume that observed lithospheric flexure, like that at the Sacramento Mountains, can be characterized by an effective elastic plate thickness (h_e). Therefore, we use a perfectly elastic plate model rather than perform simulations with a realistic but complex rheology. Second, we surmise that the finite element model including a fault is a closer approximation to reality than either the continuous or broken plate solutions. Hence, the error in h_e derived from an analytic equation fit to synthetic FEM “topography” (with a known elastic thickness) should be representative of errors in fits to real flexural topography.

4.1. Model Description

Our model of a lithosphere cut by a single master normal fault is similar in many respects to that of *Bott* [1996, 1997; also *Bott and Stern*, 1992]. We use the commercial finite element software MARC, version K6 (MARC Analysis Research Corporation, Palo Alto, California). MARC is a general-purpose engineering package applicable to structural, heat flow, and electromagnetic problems, which is readily adapted to geodynamic studies. In this paper we consider only an isotropic elastic plate cut by a throughgoing planar normal fault.

The two-dimensional, plane-strain finite element grid is comprised of four-node, isoparametric, quadrilateral elements and three-node, isoparametric, triangular elements near the fault (Figure 5). These elements use bilinear basis functions, meaning that strain is constant within each element. The grid is horizontally biased such that the mesh is finest near the fault, where the smallest elements have dimensions of 2 km. The physical properties of the plate are as given in Table 1; the plate density is $\rho_c = 2800$ kg m⁻³.

The fault is defined by a series of “gap-friction” contact elements that connect structural nodes on either side of the 2-m-wide fault. Gaps are described by a closure distance, a gap direction (normal to the fault), a shear direction (parallel to the fault), gap and shear spring stiffnesses, and a coefficient of friction. The gap stiffness is infinite to prevent the hanging wall from passing through or separating from the footwall. The shear stiffness is

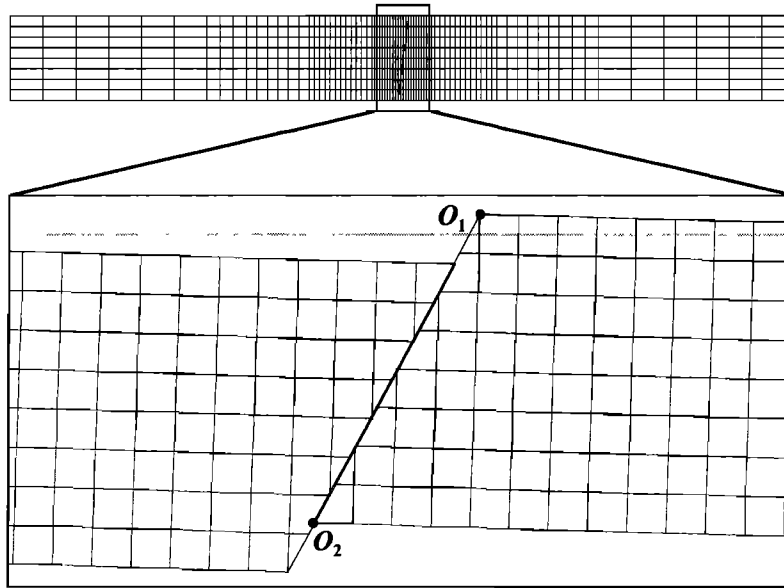


Figure 5. A complete 600-km-long, 16-km-thick finite element grid (vertically exaggerated by a factor of 4) is shown at top. Below it is a close-up of the region near the 63° fault after a heave of 1280 m, with no vertical exaggeration. (No basin infill or erosion loading applied.) Points O_1 and O_2 are alternative locations for the horizontal origin when performing analytic least-squares fits to the surface displacements.

zero for models with no friction. Mechanical problems with gap–friction elements are solved in MARC by imposing kinematic constraints and using a Lagrange multiplier method. This approach is similar to the “slippery-node” technique of *Melosh and Williams* [1989] and the “dual-node” technique of *Bott* [1997].

Restoring forces are applied by a frictionless elastic (Winkler) foundation at the base of the plate that has a stiffness $\rho_c g$. *Bott and Stern* [1992] and *Bott* [1996, 1997] placed restoring forces only at density interfaces, such as the surface. However, restoring forces exist where the mechanical lithosphere, which can sustain deviatoric stresses, is displaced in a low-viscosity, hydrostatic asthenosphere which applies a pressure to the base of the lithosphere. The depth where these buoyancy stresses occur in a viscoelastic lithosphere may vary with position and time as the state of stress and character of the material changes from solid to fluid. Nonetheless, the model foundation is properly located at the base of the mechanical lithosphere with the approximation of an inviscid asthenosphere [*Nadai*, 1963, p. 284; *Turcotte and Schubert*, 1982, pp. 121–122; *Wallace and Melosh*, 1994]. The equivalence of a basal foundation to a sublithospheric pressure-induced restoring force has been demonstrated with finite element models of flexure of an elastic plate over an explicit isoviscous substrate. In the case of a continuous, thin, elastic plate, whether the restoring forces are applied at the top or bottom surface is of no consequence, but this choice is very significant in models with a fault, as we will explain below (section 4.3).

The far left and right vertical edges of the grid are initially constrained not to move horizontally. The left edge (of the hanging wall) is “tied” to the right edge (of the footwall) such that the vertical displacements are equal on these two edges. This condition simulates an infinitely long plate and prevents prob-

lems with different net vertical motions of these two edges. Initial lithostatic stresses and gravitational body forces are applied to the grid. A horizontal extensional displacement is applied incrementally (–100 m per increment) to the left edge of the hanging wall to induce slip on the fault. We use MARC’s updated Lagrangian method (which computes the stiffness matrix at each increment using the current mesh coordinates) with the large displacement option (which accounts for large rotations). Our tests indicate that the solutions are sensitive to the large displacement effects and changes in the reference frame.

We obtain FEM solutions for a range of fault dips ($\theta = 45.0^\circ$, 63.4° , and 76.0°) and elastic plate thicknesses ($h_{\text{fem}} = 8, 16$, and 32 km). At each increment of model deformation we calculate the heave of the fault (the relative horizontal displacement of the top two fault nodes on the hanging wall and footwall). We perform a nonlinear least-squares fit of the general thin-plate elastic flexure equation (1) to the footwall surface displacements. The horizontal origin of the analytic solution is defined as the footwall cutoff (point O_1 in Figure 5). The coefficients (A and B) and flexural wavelength (λ) are varied to obtain the best fit. The best-fit line load (V_0 of equation (4)) is compared to the horizontally integrated unloading stress acting on the footwall (V_{calc}):

$$V_{\text{calc}} = (\rho_c - \rho_s) g e_0 \tan \theta \left(\frac{h_{\text{fem}}}{\tan \theta} - \frac{1}{2} e_0 \right) + V_{\text{erode}} \quad (5)$$

where e_0 is the heave and V_{erode} is the footwall erosional load (if one is applied). We define the discrepancy between the analytic and calculated loads as $V_{\text{err}} = (V_0 - V_{\text{calc}})/V_{\text{calc}}$. The best-fit elastic thickness (h_e) is compared to the true (FEM) plate thickness (h_{fem}) using the error $h_{\text{err}} = (h_e - h_{\text{fem}})/h_{\text{fem}}$. The least-squares fit is repeated for the broken plate solution by fixing the coefficient $A = 0$.

We consider three separate loading configurations: extension alone, extension with basin infill, and extension with both infill and footwall erosion. In the first case unloading of the footwall by displacement of the hanging wall provides the only driving force for flexure. We model the effect of sediment loading by applying stresses on the top surface of the hanging wall and on the exposed fault surface of the footwall where deflections are negative. The sediment has density ρ_s (Table 1) and fills the basin to the datum. In the third case we apply a uniform stress 20 km wide on the footwall that increases linearly with heave to 50 MPa at $e_0 = 1.5$ km, roughly equaling the inferred Sacramento Mountains erosional load (section 3.1, Figure 4a). This is an ad hoc treatment of erosion; the results are sensitive to the load width, magnitude, and distribution, but they should give some guidance for flexural analyses of the SM.

4.2. FEM Results

FEM model results at $e_0 = 1$ km are summarized in Tables 2–4. For all loading cases the magnitude of footwall uplift increases linearly with heave (Figure 6a), but this relationship cannot be inferred for inelastic lithospheric rheologies or listric faults. Uplift increases with fault dip because a steeper fault places more of the load closer to the footwall cutoff [e.g., *Egan*, 1992]. Uplift is relatively insensitive to plate thickness because a thicker plate produces a larger load for a given fault dip and heave (equation (5)); sensitivity to h_{fem} increases as infill and erosional loads are added. Basin sediment loading acts to reduce footwall uplift, but it increases basin subsidence. The footwall erosional load causes shallowing of or no change to the basin depths.

The discrepancy between best-fit and FEM model loads might provide insight on the relationship between the shear force derived from an elastic fit to the actual stresses acting on the rift flank. Values of V_{err} are roughly constant with heave for extension alone; with addition of infill and erosion V_{err} becomes more dependent on e_0 , but it behaves asymptotically with increasing heave (Figure 6b). The load discrepancy can be very large, although it is typically less than $\pm 50\%$ for cases in which the erosional load dominates. For all loading configurations the ratio V_0/V_{calc} increases with increasing uplift (and fault displacement). These observations hold for both the broken plate and general solutions.

The dependence of the elastic plate thickness error on heave for the different cases is similar to that of V_{err} . For models without erosion the broken plate fit systematically underestimates

h_{fem} (Tables 2 and 3 and Figures 6c and 7), and $|h_{err}|$ is inversely correlated with uplift—greater fault displacement results in more “broken” plate behavior, reducing the best-fit errors. With erosion the best-fit thickness is usually an overestimate (Table 4), and the broken plate no longer even provides a lower bound on the true elastic thickness. The ratio h_e/h_{fem} increases with both decreasing plate thickness and decreasing fault dip when erosional loading is present. In all cases errors can reach many tens of percent, and the magnitude of the broken plate h_{err} increases with addition of infill and erosion. In contrast, the general solution almost always yields thicknesses that underestimate h_{fem} by no more than $\sim 5\%$ (Tables 2–4 and Figure 7). The one exception to this statement is the case in which the erosional load width is comparable to the flexural wavelength of the 8-km plate.

We have also tested FEM models with friction on the fault surface. Fault friction has a minimal effect on the flexural behavior of an elastic plate, but this finding cannot be extended to stress-sensitive rheologies without further study.

4.3. Implications

There are several possible reasons for the analytic broken plate misfits. (1) The elastic flexure equation is derived for a thin plate, while the FEM model has a finite plate thickness and properly accounts for the vertical and shear stresses. (2) The footwall is tapered beneath the fault, while the analytic solution assumes a plate of constant thickness. (3) We have approximated distributed loads on the footwall as a single line load at the origin. (4) The edge of the footwall is not truly free because normal stresses are transmitted across the fault. The fact that the general solution returns the true FEM plate thickness despite these differences demonstrates that points 1–3 are secondary: the broken plate model fails because the zero-curvature boundary condition at the fault is inappropriate. Hanging wall infill loading enhances coupling across the fault while footwall erosion diminishes it as exemplified by the coefficient ratios A/B in Tables 2–4. When the magnitude of A/B is smaller, the plate behavior is more “broken”; there is a direct correlation between the broken plate $|h_{err}|$ and $|A/B|$.

Bott [1996] also recognized discrepancies between FEM and broken plate solutions for a faulted elastic plate. Our results differ from his in a number of important respects. The broken plate model agreed very well with *Bott*'s [1996] FEM solution when infill loading was absent; this result was a consequence of placing restoring forces at the top surface of the plate. Using origin O_2 (Figure 5) and fitting to the bottom surface where restoring forces

Table 2. FEM Results for No Infill and No Erosion at $e_0 = 1$ km

h_{fem} , km	θ , deg.	Uplift, m	Broken Plate			General Solution			
			V_{err}	h_{err}	rms, m	A/B	V_{err}	h_{err}	rms, m
8	63.4	851	+0.46	-0.07	1.08	-0.06	+0.43	-0.02	0.99
16	45.0	313	-0.66	-0.26	0.83	-0.33	-0.71	-0.03	0.12
	63.4	814	+0.05	-0.13	0.78	-0.12	-0.00	-0.04	0.42
	76.0	—	—	—	—	—	—	—	—
32	63.4	771	-0.23	-0.17	0.75	-0.18	-0.29	-0.04	0.23

For $h_{fem} = 16$ km, $\theta = 76.0^\circ$ the model fault gap elements open at $e_0 \approx 200$ m.

Table 3. FEM Results for Infill but No Erosion at $e_0 = 1$ km

h_{fem} , km	θ , deg.	Uplift, m	Broken Plate			General Solution			
			V_{err}	h_{err}	rms, m	A/B	V_{err}	h_{err}	rms, m
8	63.4	506	+1.81	-0.30	1.99	-0.40	+1.19	-0.02	0.32
16	45.0	68	-0.87	-0.76	3.36	-2.41	-1.54	-0.01	0.06
	63.4	442	+0.76	-0.39	2.27	-0.55	+0.13	-0.02	0.14
	76.0	1141	+4.81	-0.21	1.96	-0.23	+4.21	-0.05	0.65
32	63.4	371	+0.09	-0.47	2.17	-0.73	-0.53	-0.03	0.10

are applied does yield a good match between FEM and analytic displacements (Figure 7a). *Bott's* [1996] model predicted a nearly antisymmetric footwall uplift and hanging wall subsidence for no infill; the magnitudes of uplift and subsidence were the same. In contrast, our model displacements are quite different in amplitude on the footwall and hanging wall (Figure 7a). This difference is also explained by the placement of the restoring forces. For example, consider the restoring force applied to the base of the footwall beneath the fault; this force will not be fully transmitted to the hanging wall due to the decoupling effect of the fault, allowing greater basin subsidence. Basin subsidence is inhibited by placing restoring forces on the surface. The flexural deflections on the surface where the restoring forces are applied are nearly antisymmetric (Figure 7a). Thus placing restoring forces on the free surface causes overprediction of flank uplift.

Bott [1996] attempted to correct the discrepancy between FEM and analytic models with infill loading by deriving a new flexure equation subject to the requirement that the fault walls remain parallel. We have also fit *Bott's* [1996] theory to our FEM results, but find, unfortunately, that it does not correctly determine the plate thickness under almost all conditions. We find that the only way in which to elicit the elastic plate thickness from fits to the FEM deflections is to retain both the sine and cosine terms in the analytic elastic plate solution, with both coefficients as free parameters. The two coefficients depend on many of the model parameters (heave, infill density, and plate thickness), precluding any simple relationship between them. The need to retain the sine term with $A \neq B$ demonstrates that the lithosphere is neither broken nor continuous at the master fault in these models; partial coupling on a dipping fault enables an intermediate condition. Interpretation of the loads acting on the rift flank through the best-fit shear force is ambiguous for both broken plate and general solutions.

5. Elastic Flexural Fits to the Sacramento Mountains

We have found the continuous plate flexure model to be inadequate at the Sacramento Mountains (section 2, Figure 4b). In addition, plate thickness estimates based on the broken plate solution are subject to large errors according to our finite element model results (section 4.2, Tables 2–4, and Figures 6 and 7). The alternative general analytic solution is more accurate, at the cost of an additional free parameter. In this section we fit both the general and broken plate elastic flexure equations as well as the finite element model to SM topographic profiles. Our aim is to evaluate the effective elastic plate thickness (h_e) and its uncertainty using three different measures: the change in rms error as a function of h_e , the variation in h_e between different cross sections, and the sensitivity of h_e to changes in the values of fixed parameters.

We perform these fits assuming the parameter values given in Table 1. Both the plate and the substrate have density ρ_c ; the substrate density determines the restoring force. The origin (where the line load is applied) is defined by the surface trace of the fault, which we have approximated by a line trending N15°W (section 3.1). Models are fit to the residual topography (Figure 2) from the crest of the range to a distance of 200 km from the fault (the location of the Mescalero escarpment). Because of the likely contributions of erosion, salt dissolution, and collapse to Pecos Valley subsidence (section 2.7), we have also examined fits to a distance of 150 km, the base of the Pecos slope. These results, as well as fits to distances greater than 200 km, show only minor changes to the inferred h_e (less than ~ 2 km).

We first evaluate the accuracy of the elastic plate fits by examining the variation in rms misfit between the analytic equations and the observed topography (33°N profile) as a function of h_e .

Table 4. FEM Results for Infill and Erosion at $e_0 = 1$ km

h_{fem} , km	θ , deg.	Uplift, m	Broken Plate			General Solution			
			V_{err}	h_{err}	rms, m	A/B	V_{err}	h_{err}	rms, m
8	63.4	1091	-0.11	+0.91	3.98	+0.53	-0.02	+0.28	1.24
16	45.0	476	-0.45	+0.63	1.64	+0.64	-0.39	+0.03	0.19
	63.4	789	-0.33	+0.14	0.83	+0.18	-0.29	-0.01	0.29
	76.0	1499	+0.19	+0.04	1.09	+0.07	+0.22	-0.02	0.86
32	63.4	605	-0.38	-0.13	0.36	-0.10	-0.40	-0.05	0.20

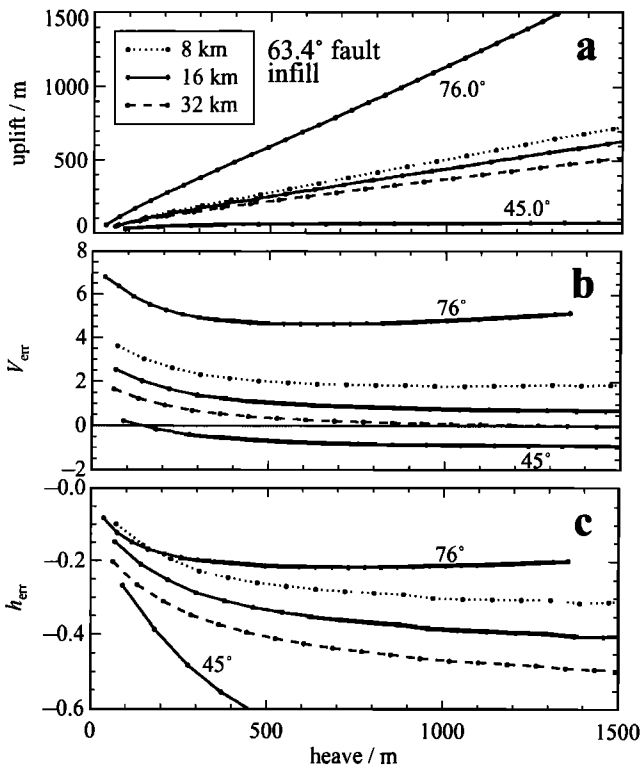


Figure 6. Effects of varying elastic plate thickness and fault dip on finite element results as a function of heave. Basin infill loading is included; denudational loading is not. Symbols mark 100-m increments of displacement at the far left edge of the hanging wall. (a) Maximum FEM footwall uplift. (b) Line load discrepancy (V_{err}) between analytic broken plate shear force and integrated load estimated from kinematic description of footwall unloading (equation (5)). (c) Fractional error in elastic plate thickness derived by broken plate analytic fit to FEM displacements relative to true FEM plate thickness (h_{err}). Broken plate origin defined at point O_1 in Figure 5. Compare Table 3.

We fix the datum elevation at -129 m, the height of the Southern High Plains in the residual topography (Figure 2d). We systematically vary the flexural wavelength. For the general solution and the broken plate equation we vary the cosine coefficient (B) to match the elevation of the crest; for the general solution we also perform a least squares fit to determine the sine coefficient (A). The results are shown in Figure 8. There is a fairly sharp lower bound on h_e of ~ 15 km from the general solution, and a much weaker constraint on the upper bound. The broken plate has a very pronounced minimum in rms error between $h_e \approx 18$ km and 25 km, and visual examination of the fits also shows that this is the most acceptable range of plate thicknesses.

The comparison of the general and broken plate solutions at the SM indicates that we can only establish a lower bound on the effective elastic thickness with an analytic model. This finding is consistent with the simulated broken plate FEM tests for h_{fem} greater than ~ 20 km (Table 4). Figure 9 shows a finite element model flexural profile for $h_{fem} = 20$ km and $\theta = 63.4^\circ$ which provides a good fit to the SM. Greater plate thicknesses cause longer wavelength flexure, misfitting the Pecos slope. Thus, for this case of high-amplitude (~ 1 -km) uplift the broken plate h_{err} is

small, as seen in the simulations (Tables 2–4). The broken plate solution should provide accurate estimates of the elastic thickness and its uncertainty at the SM.

Next we fit the broken plate equation to 22 east–west profiles, from 32.76°N to 33.13°N , spaced about 2 km apart in latitude. The datum is a free parameter in the least squares analysis, along with the flexural wavelength and cosine coefficient. The mean elastic thickness of these 22 fits is 23.0 ± 2.3 km, ranging from 20.7 to 29.3 km. There is surprisingly little variation in h_e along strike of the range, despite the irregular topography on the Pecos slope. The standard deviation amounts to only 10% of h_e . Best-fit loads are about 1×10^{12} N m^{-1} .

We have also carried out sensitivity tests to determine the effect of parameter uncertainties on h_e . The parameters of concern are the datum elevation, the location of the origin, the

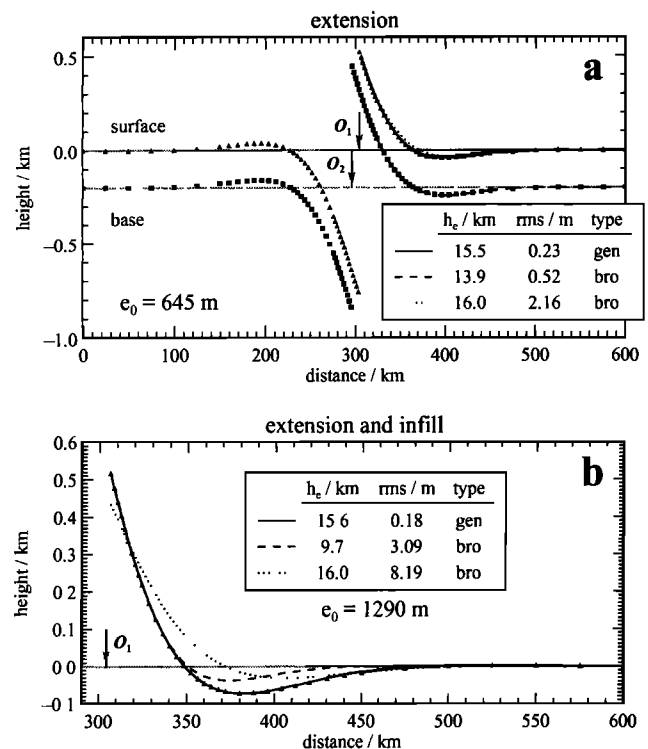


Figure 7. Analytic elastic plate equation least-squares fits to finite element model deflection profiles for a 16-km-thick plate with a 63.4° fault. Three cases are illustrated: the generalized equation (“gen”) as well as the broken plate equation (“bro”) with the elastic plate thickness a free parameter (dashed line) or fixed at 16 km (dotted line). Origins assumed for fits are marked by arrows (see Figure 5). (a) FEM model without basin infill loading; deflections at the surface (triangles) and base (squares) of the FEM plate are plotted. Latter profile is offset -200 m vertically for clarity. It is nearly antisymmetric across the fault, while the magnitude of surface footwall uplift is considerably less than the magnitude of surface hanging wall subsidence. The generalized and broken plate fits are indistinguishable on the plot. The broken plate solution with a forced 16-km thickness is acceptable, despite the much higher rms error. The broken plate fit to the base of the plate where the restoring forces are applied (with the origin at point O_2) produces an excellent fit ($h_e = 16.1$ km, rms = 0.32 m). (b) Same FEM model, but now including basin infill loading. The surface deflections of only the footwall are shown. In this case the broken plate fits are considerably worse.

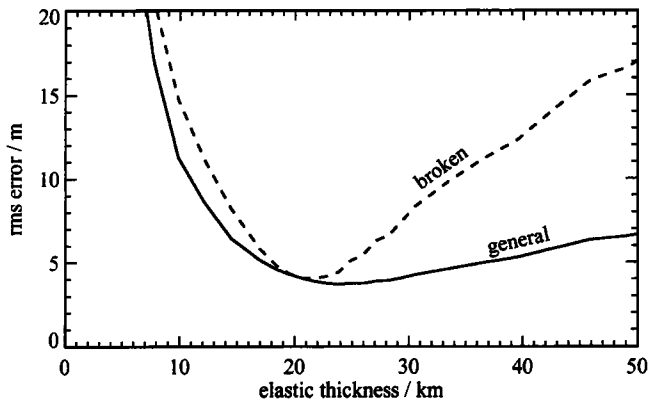


Figure 8. Root mean square (rms) misfit as a function of plate thickness for analytic elastic flexural fits to Sacramento Mountains residual topographic profile at 33°N (Figure 2). Solid curve corresponds to fits with the general solution, and the dashed curve corresponds to the broken plate solution. The minima for these two methods are the same, indicating the broken plate equation gives, at worst, a lower limit on h_e .

substrate density (restoring force stiffness), Young's modulus, and Poisson's ratio. We treat each of these in turn; the results of these tests are summarized in Table 5. The "nominal" model comprises a least squares fit of the broken plate with the cosine coefficient varied to best match the SM amplitude and with the datum and flexural wavelength free; it is plotted in Figure 9.

The appropriate datum for the differenced profile is not obvious (Figure 2d). Perhaps it is at zero residual elevation, where the SM profile and the averaged profile are at the same elevation (i.e., on the Great Plains, about 500 km from the SM). Or perhaps it belongs at the surface of the Pecos Valley (~150 km from the SM), at a residual elevation of ~-250 m. We find that these extremes for the reference elevation are not acceptable, resulting in large misfits to the Pecos Valley. The best fit datum is -129 m (the residual elevation of the Southern High Plains), and we consider a smaller range of -75 to -175 m. Even these datums produce flexural profiles that compare very poorly to the Pecos Valley, which would imply that it formed later, and by an entirely different process, than the young SM uplift. The Pecos Valley is a flexural downwarp for the -129-m datum (Figure 9). Nonetheless, these changes to the datum result in only ~10% changes in h_e .

The proper location of the horizontal origin, defined by the surface trace of the fault, is uncertain because of our linear approximation to the sinuous map trace and because multiple faults probably accommodated the SM uplift. We take the origin uncertainty to be ± 5 km, yielding a <10% variation in h_e .

We have assumed that the lithosphere is confined to the crust, but the effective elastic thickness of ~20 km does not correspond to a true mechanical lithosphere thickness, which is undoubtedly greater accounting for frictional weakening near the surface and viscous creep at depth. Given a crustal thickness of ~30–50 km [Keller et al., 1990; Roberts et al., 1991], the lithosphere may include the upper mantle. Due to this uncertainty, we consider a mantle substrate density of 3300 kg m^{-3} , which determines the magnitude of the buoyant restoring forces. This higher density causes only a 5% change in the predicted h_e .

Altering Young's modulus and Poisson's ratio does not modify the elastic flexural fits. These parameters do, however, affect the conversion of flexural wavelength to elastic thickness. We have assumed a value of $E = 65 \text{ GPa}$, representative of literature values for crustal rocks, but Young's modulus can vary by over a factor of 10 with rock type [Turcotte and Schubert, 1982, p. 432]. Changing E by ~50% can dramatically influence the derived value of h_e , from -13% to +31%. The elastic thickness is not sensitive to modest changes in Poisson's ratio.

6. Discussion and Conclusions

6.1. Rio Grande Rift Flank Tectonics

One goal of this research has been to identify synrift flank uplifts at the Rio Grande rift. While there are several examples of such uplifts, flexural footwall uplifts amenable to modeling are elusive. RGR flanks are very complex, reflecting their prolonged tectonic history (particularly Laramide deformation)—a fact apparent in the geology, topography, and apatite fission track measurements of the ranges. Those flanks with only small components of Laramide relief and the strongest evidence for rapid late Tertiary uplift—the Sandia Mountains, the Sierra Lucero, Ladron Peak, the Lemitar Mountains—are so pervasively faulted that models assuming mechanical continuity of the lithosphere are inappropriate. These uplifts stand apart even from Basin and Range metamorphic core complexes [e.g., Davis and Lister, 1988], which formed in very weak crust but have been modeled assuming a continuous lithosphere [Buck, 1988; Wdowinski and Axen, 1992]. For example, fitting the broken elastic plate analytic flexure equation to the Sandia Mountains yields an elastic thickness of only ~1 km, an implausible result given the seismic reflection observations of brittle faulting to depths of ~10 km in the Albuquerque Basin [Russell and Snelson, 1994]. The lithosphere is so highly bent in this fit that some of the assumptions of the analysis are not justifiable.

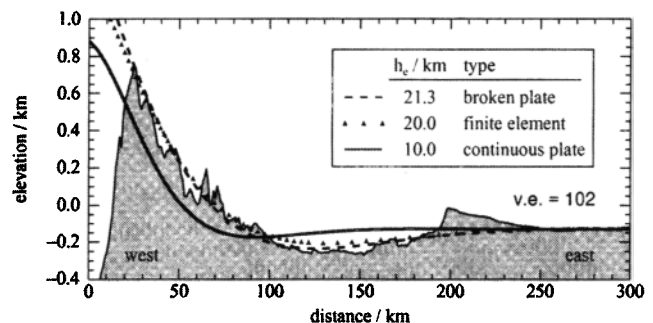


Figure 9. Residual Sacramento Mountains topography at 33°N (Figure 2d) with nominal broken elastic plate fit. The origin, near the surface trace of the master fault, is at the left edge of the plot. In this model, the flexural wavelength, line load (or cosine coefficient), and vertical datum are free parameters. The best fit values of these variables are 53.3 km ($h_e = 21.3 \text{ km}$), $1.2 \times 10^{12} \text{ N m}^{-1}$, and -129 m, respectively. The line load was constrained by the requirement that the solution pass through the range crest. The triangles mark the nodal displacements of a similar FEM solution, with $h_{\text{fem}} = 20 \text{ km}$, $\theta = 63.4^\circ$, $e_0 = 1.8 \text{ km}$, and a denudational line load of $1.2 \times 10^{12} \text{ N m}^{-1}$. Also shown is a continuous plate solution with a distributed load comparable to the stresses applied to the FEM model.

Table 5. Flexure Sensitivity Test Results

Parameter	Value	Change*, %	h_e , km	h_e Change*, %	rms, m
Nominal model†	—	—	21.3	—	4.04
Datum	-75 m	+42	19.5	-8	5.42
	-175 m	-36	23.7	+12	4.89
Origin	-5 km	—	22.9	+8	3.86
	+5 km	—	20.2	-5	4.25
Substrate density	3300 kg m ⁻³	+18	22.4	+5	4.34
Young's modulus	100 GPa	+54	18.6	-13	4.02
	30 GPa	-54	27.8	+31	4.02
Poisson's ratio	0.20	-20	21.6	+2	4.02
	0.30	+20	21.2	-0.1	4.02

* Change in parameter value or elastic plate thickness relative to nominal model.

† For the nominal model (33°N Sacramento Mountains residual topographic cross section), the datum elevation is -129 m, the horizontal origin is defined as 0 km, the restoring force stiffness is $\rho_0 g$, and all other parameters are as in Table 1.

The Sacramento Mountains (SM) in southeastern New Mexico are the only compelling example of flexural flank uplift. This range exhibits structural continuity both along strike and perpendicular to strike, legitimizing application of continuum mechanical models of the footwall. Several lines of evidence support an interpretation of synrift uplift little affected by Laramide deformation (section 2.6). The SM gradually increase in slope from the Pecos Valley to the crest, indicative of flexural uplift of a "broken" plate. Our focus has therefore been on flexural modeling of rift flank uplift at the SM.

6.2. Rift Flank Flexure Modeling

Further objectives of this work have been to understand the consequences of alternative boundary conditions and uplift mechanisms, as well as the sensitivity of flexure solutions to modeling approximations and parameter values. Arguably the worst supposition one could make when studying rift flank uplifts is that all the topographic relief is attributable to a single mechanism. We assert that it is essential to differentiate between relief arising from shallow, narrow loads (basins, erosion, faulting) and deep, wide loads (necking, compositional and thermal density anomalies). The former component of topography is potentially flexural and may avail itself to determination of lithospheric thickness; the latter is less well understood and provides poor constraints on lithospheric thickness. We accomplish separation of these components by subtracting the broad, unfaulted flank topography of the Mescalero arch from the SM cross sections (Figure 2).

This step is crucial: it alone is responsible for a factor of 2 decrease in estimated broken elastic plate thickness from 42 km (section 3.1) to a nominal 21 km (section 5). By extracting the short-wavelength flank topography we presumably remove longer wavelength components of uplift not specifically associated with normal faulting and basin formation, including topography arising from lateral heat conduction, small-scale convection, dynamic flow stresses, and lithospheric necking [Alvarez *et al.*, 1984; Buck, 1986; Zuber and Parmentier, 1986; Chéry *et al.*, 1992]. However, it is more common to explain all uplift at a rift flank with one mechanism alone [e.g., Steckler, 1985; Villemin *et al.*, 1986; Ebinger *et al.*, 1991]. We suggest that such models are prone to errors in estimates of lithospheric structure and driving stresses responsible for rift topography.

We have also identified problems with the continuous plate assumption in modeling flexural rift flank uplift. This model does not just predict an incorrect lithospheric thickness, it is seemingly unable to explain the Sacramento Mountains topography at all without special pleading (Figure 4b). Although we have liberally overestimated the applied loads, no elastic plate thickness can reproduce the position and amplitude of the SM; we return to this problem below. The continuous plate premise is common in the literature [Weissel and Karner, 1989; Ebinger *et al.*, 1991; Kuszniir *et al.*, 1991; Egan, 1992; Kuszniir and Ziegler, 1992]; again, we must question the results of such models.

With our finite element modeling (FEM) of flexure accompanying slip on a normal fault, we have examined the approximations inherent to analytic thin-plate flexure models that treat the fault only as a boundary condition, and we have estimated the errors in lithospheric thickness and applied loads associated with these simpler models. We emphasize that the restoring forces must be applied at the base of the lithosphere, not the surface (section 4.1); incorrect placement of the restoring forces results in erroneous flexural deflections (section 4.3). Our FEM simulations with and without basin infill, but no erosion, indicate that broken elastic plate fits to rift flank topography underestimate "true" elastic lithosphere thicknesses by tens of percent, the exact discrepancy depending primarily on the fault dip and plate thickness (Figure 6). A modified boundary condition proposed by Bott [1996] does not account for these errors. The inclusion of a foot-wall erosional load reveals large broken plate thickness errors that can be either positive or negative (Table 4). Therefore, the broken plate boundary assumption, employed by several workers [e.g., Stern and ten Brink, 1989; Bott and Stern, 1992; Masek *et al.*, 1994], is also generally not accurate.

A fundamental conclusion of this work is that the continuous and broken plate analytic rift flank flexure models cannot even provide consistent lower or upper bounds on the effective elastic lithosphere thickness. Interpretation of the loads acting on the flank are equally ambiguous. These shortcomings leave two alternatives. One may use the general flexure equation (1) with (at least) three free parameters: the coefficients (A and B) and the flexural wavelength (λ). In principle, B is fixed by the amplitude of the uplift and A and λ are determined by the combination of the back slope of the uplift and the location of the peripheral trough. However, peripheral troughs are not commonly recognized adjacent to rift flanks, and the applied forces derived from

this model are also uninformative. The second choice is to explicitly model the fault as is done here (section 4) and by a few other workers [King and Ellis, 1990; Bott, 1997], which, while more physically robust, is a much less expedient alternative.

6.3. Sacramento Mountains Flexure

At the Sacramento Mountains we find that the broken plate solution does give a reasonable estimate of the effective elastic thickness because the large amplitude of the uplift causes significant decoupling across the fault (Figures 8 and 9). To test for sources of uncertainty in rift flank flexure, we have fit the broken plate equation to 22 SM profiles varying all relevant parameters. The effective elastic thickness (h_e) along strike is a surprisingly consistent 23.0 ± 2.3 km. The elastic thickness is subject to error on the <10% level for most fitting and physical parameters (Table 5), with the exception of Young's modulus, which potentially introduces a ~30% error. We cannot state with certainty what the net effect of all these errors might be. Perhaps 50% is a reasonable upper bound, corresponding to about ± 12 km for the SM. The errors arising from parameter uncertainties are typically less than those from the fault boundary condition approximations for moderate flank uplifts (<1 km).

Our mean elastic plate thickness estimate for the SM, $h_e \approx 23$ km, is comparable to that of Lowry and Smith [1994] for the Archean Wyoming craton and northwest Colorado Plateau, and greater than their and Stein *et al.*'s [1988] values for the Basin and Range. It agrees with the spectrally derived thickness of Bechtel *et al.* [1990] for the RGR region, and seems to be appropriate for an area between the rift axis and the craton. Sacramento Mountains uplift and Pecos River Valley downwarping initiated in the late Miocene (<12 Ma); these events are associated with late-phase RGR extension, and they are probably recent. Our model of the SM implies that the Pecos Valley is a flexural trough (Figure 9). This result is supported by geologic information on the valley formation (section 2.7), although salt dissolution and erosion have also contributed to the observed subsidence. Rift tectonics probably controlled the development of both the Rio Grande and Pecos drainages.

The load balance for the SM is not easily interpreted using the shear force derived from analytic fits, as indicated by the FEM simulations. A direct FEM model of the flank uplift is required to ascertain if the model-derived loads match the geologically inferred stresses. An FEM model fit with $h_{fem} = 20$ km and $\theta = 63^\circ$ (Figure 9) requires $e_0 = 1.8$ km and a 1.2×10^{12} N m⁻¹ denudational force, exceeding the inferred heave and erosion (section 3.3). This result implies that we have not recognized all the loads present at the SM; the $\sim 5 \times 10^{11}$ N m⁻¹ "missing" force is ~50% of the net estimated load. The continuous plate model was rejected for its inability to match the SM topography with "known" driving stresses, but the need for additional forces in the faulted-plate model obliges us to reconsider this judgement. If the additional stresses are applied to a continuous plate, a large misfit with the SM persists (Figure 9). However, our ignorance of the driving stresses leaves open the possibility of a still larger "missing" load that would allow the continuous plate solution to

be acceptable. We conclude that the faulted plate model is preferable because it better accounts for the physics of a faulted upper crust and minimizes the anomalous stresses at the SM, but we cannot firmly reject the continuous plate approach. In any case, the contribution of erosion is important, and probably dominant, in the SM flexure.

6.4. Improved Rift Flank Modeling

Another aspiration of this study has been to advance beyond effective elastic thickness estimates to more relevant assessments of the lithospheric geotherm, which can then be compared to surface heat flow measurements or thermal structure inferred from xenolith geothermobarometry. Two methods that might be used to achieve geotherm estimates rely on constructing yield strength envelopes for the continental lithosphere [Kohlstedt *et al.*, 1995]. One approach is to take the maximum bending curvature and moment from an elastic fit and find the geotherm that gives an equivalent moment for an elastic-plastic lithosphere (in which the bending stresses are limited by the yield strength envelope) [McNutt and Menard, 1982; Mueller and Phillips, 1995]. Alternatively, one could generate the nonlinear moment-curvature function from the yield strength envelope and numerically solve the flexure equation with a finite difference routine [Brown and Grimm, 1996].

We have fit broken plate elastic-plastic flexural models to the SM flank uplift and find that the simpler moment-curvature matching technique is very accurate when compared to complete forward models. The maximum bending curvature ($\sim 4 \times 10^{-7}$ m⁻¹) is predicted to occur on the Pecos slope, ~40 km east of the fault. However, the uncertainties in both the yield strength envelope and fitting parameters (i.e., datum, origin) produce a very large geotherm uncertainty, from 10 to 30 K km⁻¹. The most that can be said about these results is that they are consistent with heat flow [Reiter *et al.*, 1986] and xenolith [Bussod and Williams, 1991] information.

The future direction of rift flank modeling must be toward a more realistic representation of faulting within the lithosphere. While we favor the broken over the continuous plate model, the truth may lie somewhere in between. Bott [1997] included plasticity in his plate, but he neglected the role of viscous creep in the lower lithosphere. Our model, too, implicitly assumes penetrative faulting of the mechanically competent lithosphere and inviscid flow beneath this layer. But we recognize the nature of extension must transition from simple-shear normal faulting in the upper crust to pure-shear stretching or necking in the lower crust and upper mantle, and the mechanical response of the viscous lithosphere will influence the deformation and uplift observed at the surface [e.g., Chéry *et al.*, 1992]. The challenge is to satisfactorily simulate intralithospheric faults in the finite element model without introducing singularities or space problems [cf. Melosh and Williams, 1989; Boutilier and Keen, 1994].

Acknowledgments. We thank Michael Steckler, Scott Baldrige, and associate editor Carolyn Ruppel for their thorough reviews. This work was supported in part by NASA grant NAGW-3024 and NSF grant EAR-9706140.

References

- Adams, D. C., and G. R. Keller, Crustal structure and basin geometry in south-central New Mexico, in *Basins of the Rio Grande Rift: Structure, Stratigraphy, and Tectonic Setting*, edited by G. R. Keller and S. M. Cather, *Spec. Pap. Geol. Soc. Am.*, 291, 241–255, 1994.
- Alvarez, F., J. Virieux, and X. Le Pichon, Thermal consequences of lithosphere extension over continental margins: The initial stretching phase, *Geophys. J. R. Astron. Soc.*, 78, 389–411, 1984.
- Bachman, G. O., Cenozoic deposits of southeastern New Mexico and an outline of the history of evaporite dissolution, *J. Res. U. S. Geol. Surv.*, 4, 135–149, 1976.
- Baldrige, W. S., Y. Bartov, and A. Kron, Geologic map of the Rio Grande rift and southeastern Colorado Plateau, New Mexico and Arizona, scale 1:500,000, in *Rio Grande Rift: Tectonics and Magmatism*, edited by R. E. Riecker, AGU, Washington, D. C., 1983.
- Baldrige, W. S., G. R. Keller, V. Haak, E. Wendlandt, G. R. Jiracek, and K. H. Olsen, The Rio Grande rift, in *Continental Rifts: Evolution, Structure, Tectonics*, edited by K. H. Olsen, pp. 233–275, Elsevier, New York, 1995.
- Bartsch-Winkler, S., Geology of east-central New Mexico, in *Mineral and Energy Resources of the Roswell Area, East-Central New Mexico*, edited by S. Bartsch-Winkler and A. J. Donatich, *U. S. Geol. Surv. Bull.*, 2063, 5–34, 1995.
- Bechtel, T. D., D. W. Forsyth, V. L. Sharpton, and R. A. F. Grieve, Variations in effective elastic thickness of the North American lithosphere, *Nature*, 343, 636–638, 1990.
- Bott, M. H. P., Flexure associated with planar faulting, *Geophys. J. Int.*, 126, F21–F24, 1996.
- Bott, M. H. P., Modeling the formation of a half graben using realistic upper crustal rheology, *J. Geophys. Res.*, 102, 24,605–24,617, 1997.
- Bott, M. H. P., and T. A. Stern, Finite element analysis of Transantarctic Mountain uplift and coeval subsidence in the Ross Embayment, *Tectonophysics*, 201, 341–356, 1992.
- Boutlier, R. R., and C. E. Keen, Geodynamic models of fault-controlled extension, *Tectonics*, 13, 439–454, 1994.
- Bowsher, A. L., Some effects of Precambrian basement on the development of the Sacramento Mountains, in *Geology of the Sierra Blanca, Sacramento and Capitan Ranges, New Mexico*, edited by J. M. Barker, B. S. Kues, G. S. Austin, and S. G. Lucas, *Field Conf. Guideb. N. M. Geol. Soc.*, 42, 81–89, 1991.
- Bridwell, R. J., and C. A. Anderson, Thermomechanical models of the Rio Grande rift, in *Mechanisms of Continental Drift and Plate Tectonics*, edited by P. A. Davies and S. K. Runcorn, pp. 41–59, Academic, San Diego, Calif., 1980.
- Brister, B. S., and R. R. Gries, Tertiary stratigraphy and tectonic development of the Alamosa Basin (northern San Luis Basin), Rio Grande rift, south-central Colorado, in *Basins of the Rio Grande Rift: Structure, Stratigraphy, and Tectonic Setting*, edited by G. R. Keller and S. M. Cather, *Spec. Pap. Geol. Soc. Am.*, 291, 39–58, 1994.
- Brown, C. D., and R. E. Grinn, Lithospheric rheology and flexure at Artemis Chasma, Venus, *J. Geophys. Res.*, 101, 12,697–12,708, 1996.
- Buck, W. R., Small-scale convection induced by passive rifting: The cause for uplift of rift shoulders, *Earth Planet. Sci. Lett.*, 77, 362–372, 1986.
- Buck, W. R., Flexural rotation of normal faults, *Tectonics*, 7, 959–973, 1988.
- Burchfiel, B. C., D. S. Cowan, and G. A. Davis, Tectonic overview of the Cordilleran orogen in the western United States, in *The Geology of North America*, vol. G3, *The Cordilleran Orogen: Conterminous U. S.*, edited by B. C. Burchfiel, P. W. Lipman, and M. L. Zoback, pp. 407–479, Geol. Soc. of Am., Boulder, Colo., 1992.
- Bussod, G. Y. A., and D. R. Williams, Thermal and kinematic model of the southern Rio Grande rift: Inferences from crustal and mantle xenoliths from Kilbourne Hole, New Mexico, *Tectonophysics*, 197, 373–389, 1991.
- Caran, S. C., Cenozoic stratigraphy, southern Great Plains and adjacent areas, in *The Geology of North America*, vol. K2, *Quaternary Nonglacial Geology: Conterminous U. S.*, edited by R. B. Morrison, plate 5, Geol. Soc. of Am., Boulder, Colo., 1991.
- Chapin, C. E., and S. M. Cather, Tectonic setting of the axial basins of the northern and central Rio Grande rift, in *Basins of the Rio Grande Rift: Structure, Stratigraphy, and Tectonic Setting*, edited by G. R. Keller and S. M. Cather, *Spec. Pap. Geol. Soc. Am.*, 291, 5–25, 1994.
- Chapin, C. E., and W. R. Seager, Evolution of the Rio Grande rift in the Socorro and Las Cruces areas, in *Guidebook of the Las Cruces Country*, edited by W. R. Seager, R. E. Clemens, and J. F. Callender, *Field Conf. Guideb. N. M. Geol. Soc.*, 26, 297–321, 1975.
- Chéry, J., F. Lucazeau, M. Daignières, and J. P. Vilotte, Large uplift of rift flanks: A genetic link with lithospheric rigidity?, *Earth Planet. Sci. Lett.*, 112, 195–211, 1992.
- Coney, P. J., Structure, volcanic stratigraphy, and gravity across the Mogollon Plateau, New Mexico, in *Cenozoic Volcanism in Southwestern New Mexico*, edited by W. E. Elston and S. A. Northrop, *Spec. Publ. N. M. Geol. Soc.*, 5, 29–41, 1976.
- Cordell, L., Extension in the Rio Grande rift, *J. Geophys. Res.*, 87, 8561–8569, 1982.
- Davis, G. A., and G. S. Lister, Detachment faulting in continental extension; Perspectives from the southwestern U.S. Cordillera, in *Processes in Continental Lithospheric Deformation*, edited by S. P. Clark, B. C. Burchfiel, and J. Suppe, *Spec. Pap. Geol. Soc. Am.*, 218, 133–159, 1988.
- Davis, P. M., Continental rift structures and dynamics with reference to tectonic studies of the Rio Grande and East African rifts, *Tectonophysics*, 197, 309–325, 1991.
- Eaton, G. P., Topography and origin of the southern Rocky Mountains and Alvarado Ridge, in *Continental Extensional Tectonics*, edited by M. P. Coward, J. F. Dewey, and P. L. Hancock, *Spec. Publ. Geol. Soc.*, 28, 355–369, 1987.
- Ebinger, C. J., G. D. Karner, and J. K. Weissel, Mechanical strength of extended continental lithosphere: Constraints from the western rift system, East Africa, *Tectonics*, 10, 1239–1256, 1991.
- Egan, S. S., The flexural isostatic response of the lithosphere to extensional tectonics, *Tectonophysics*, 202, 291–308, 1992.
- Epis, R. C., and C. E. Chapin, Geomorphic and tectonic implications of the post-Laramide, late Eocene erosion surface in the southern Rocky Mountains, in *Cenozoic History of the Southern Rocky Mountains*, edited by B. F. Curtis, *Mem. Geol. Soc. Am.*, 144, 45–74, 1975.
- Frye, J. C., A. B. Leonard, and H. D. Glass, Western extent of Ogallala Formation in New Mexico, *Circ.*, 175, 41 pp., N. M. Bur. Mines Min. Resour., Socorro, 1982.
- Gilchrist, A. R., and M. A. Summerfield, Differential denudation and flexural isostasy in formation of rifted-margin upwarps, *Nature*, 346, 739–742, 1990.
- Gregory, K. M., and C. G. Chase, Tectonic and climatic significance of a late Eocene low-relief, high-level geomorphic surface, Colorado, *J. Geophys. Res.*, 99, 20,141–20,160, 1994.
- Gustavson, T. C., and R. J. Finley, Late Cenozoic geomorphic evolution of the Texas Panhandle and northeastern New Mexico, *Rep. of Invest.*, 148, 42 pp., Bur. of Econ. Geol., Univ. of Tex., Austin, 1985.
- Gustavson, T. C., V. T. Holliday, and G. E. Schultz, Introduction, in *Tertiary and Quaternary Stratigraphy and Vertebrate Paleontology of Parts of Northwestern Texas and Eastern New Mexico*, edited by T. C. Gustavson, *Tex. Bur. Econ. Geol. Guideb.*, 24, 1–21, 1990.
- Harrison, R. W., Winston graben: Stratigraphy, structure, and tectonic setting, in *Basins of the Rio Grande Rift: Structure, Stratigraphy, and Tectonic Setting*, edited by G. R. Keller and S. M. Cather, *Spec. Pap. Geol. Soc. Am.*, 291, 227–240, 1994.
- Heywood, C. E., Isostatic residual gravity anomalies of New Mexico, *U. S. Geol. Surv. Water Resour. Invest. Rep.*, 91–4065, 27 pp., 1992.
- Ingersoll, R. V., W. Cavazza, W. S. Baldrige, and M. Shafiqullah, Cenozoic sedimentation and paleotectonics of north-central New Mexico: Implications for initiation and evolution of the Rio Grande rift, *Geol. Soc. Am. Bull.*, 102, 1280–1296, 1990.
- Keller, G. R., L. Cordell, G. H. Davis, W. J. Peeples, and G. White, A geophysical study of the San Luis basin, in *Rio Grande Rift: Northern New Mexico*, edited by W. S. Baldrige, P. W. Dickerson, R. E. Riecker, and J. Zidek, *Field Conf. Guideb. N. M. Geol. Soc.*, 35, 51–57, 1984.
- Keller, G. R., P. Morgan, and W. R. Seager, Crustal structure, gravity anomalies and heat flow in the southern Rio Grande rift and their relationship to extensional tectonics, *Tectonophysics*, 174, 21–37, 1990.
- Keller, G. R., M. A. Khan, P. Morgan, R. F. Wendlandt, W. S. Baldrige, K. H. Olsen, C. Prodehl, and L. W. Braile, A comparative study of the Rio Grande and Kenya rifts, *Tectonophysics*, 197, 355–371, 1991.
- Kelley, S. A., and C. E. Chapin, Cooling histories of mountain ranges in the southern Rio Grande rift based on apatite fission-track analysis—A reconnaissance survey, *N. M. Geol.*, 19, 1–14, 1997.
- Kelley, S. A., and I. J. Duncan, Late Cretaceous to middle Tertiary tectonic history of the northern Rio Grande rift, New Mexico, *J. Geophys. Res.*, 91, 6246–6262, 1986.
- Kelley, S. A., C. E. Chapin, and J. Corrigan, Late Mesozoic to Cenozoic cooling histories of the flanks of the northern and central Rio Grande rift, Colorado and New Mexico, *Bull.*, 145, 40 pp., N. M. Bur. Mines Min. Resour., Socorro, 1992.
- Kelley, V. C., Geology of the Pecos Country, southeastern New Mexico, *Mem.*, 24, 75 pp., N. M. Bur. Mines Min. Resour., Socorro, 1971.
- Kelley, V. C., Tectonics, middle Rio Grande rift, New Mexico, in *Rio Grande Rift: Tectonics and Magmatism*, edited by R. E. Riecker, pp. 57–70, AGU, Washington, D. C., 1979.
- Kelley, V. C., and S. A. Northrop, Geology of Sandia Mountains and vicinity, New Mexico, *Mem.*, 29, 136 pp., N. M. Bur. Mines Min. Resour., Socorro, 1975.
- King, G., and M. Ellis, The origin of large local uplift in extensional regions, *Nature*, 348, 689–693, 1990.
- Kohlstedt, D. L., B. Evans, and S. J. Mackwell, Strength of the lithosphere: Constraints imposed by laboratory experiments, *J. Geophys. Res.*, 100, 17,587–17,602, 1995.
- Kooi, H., S. Cloetingh, and J. Burrus, Lithospheric necking and regional isostasy at extensional basins, I., Subsidence and gravity modeling with an application to the Gulf of Lions margin (SE France), *J. Geophys. Res.*, 97, 17,553–17,571, 1992.
- Kusznir, N. J., and P. A. Ziegler, The mechanics of continental extension and sedimentary basin formation: A simple-shear/pure-shear flexural cantilever model, *Tectonophysics*, 215, 117–131, 1992.
- Kusznir, N. J., G. Marsden, and S. S. Egan, A flexural-cantilever simple-shear/pure-shear model of continental lithosphere extension: Applications to the Jeanne d'Arc Basin, Grand Banks and Viking Graben, North Sea, in *The Geometry of Normal*

- Faults*, edited by A. M. Roberts, G. Yielding, and B. Freeman, *Spec. Publ. Geol. Soc.*, 56, 41–60, 1991.
- Lewis, C. J., and W. S. Baldrige, Crustal extension in the Rio Grande rift, New Mexico: Half-grabens, accommodation zones, and shoulder uplifts in the Ladron Peak–Sierra Lucero area, in *Basins of the Rio Grande Rift Structure, Stratigraphy, and Tectonic Setting*, edited by G. R. Keller and S. M. Cather, *Spec. Pap. Geol. Soc. Am.*, 291, 135–155, 1994.
- Lowry, A. R., and R. B. Smith, Flexural rigidity of the Basin and Range–Colorado Plateau–Rocky Mountain transition from coherence analysis of gravity and topography, *J. Geophys. Res.*, 99, 20, 123–20, 140, 1994.
- Lozinsky, R. P., Cross section across the Jornada del Muerto, Engle, and northern Palomas Basins, south-central New Mexico, *N. M. Geol.*, 9, 55–63, 1987.
- Lozinsky, R. P., and P. W. Bauer, Structure and basin-fill units of the Tularosa basin, in *Geology of the Sierra Blanca, Sacramento and Capitan Ranges, New Mexico*, edited by J. M. Barker, B. S. Kues, G. S. Austin, and S. G. Lucas, *Field Conf. Guideb. N. M. Geol. Soc.*, 42, 7–9, 1991.
- Machette, M. N., Preliminary assessment of paleoseismicity at White Sands Missile Range, southern New Mexico—Evidence for recency of faulting, fault segmentation, and repeat intervals for major earthquakes in the region, *U. S. Geol. Surv. Open File Rep.*, 87-444, 46 pp., 1987.
- Masek, J. G., B. L. Isacks, E. J. Fielding, and J. Bröwaey, Rift flank uplift in Tibet. Evidence for a viscous lower crust, *Tectonics*, 13, 659–667, 1994.
- May, S. J., S. A. Kelley, and L. R. Russell, Footwall unloading and rift shoulder uplifts in the Albuquerque Basin. Their relation to syn-rift fanglomerates and apatite fission-track ages, in *Basins of the Rio Grande Rift: Structure, Stratigraphy, and Tectonic Setting*, edited by G. R. Keller and S. M. Cather, *Spec. Pap. Geol. Soc. Am.*, 291, 125–134, 1994.
- McGookey, D. A., T. C. Gustavson, and A. D. Hoadley, *Regional Structural Cross Sections. Mid-Permian to Quaternary Strata, Texas Panhandle and Eastern New Mexico*, 17 pp., 14 plates, Tex. Bur. of Econ. Geol., Austin, 1988.
- McNutt, M. K., Lithospheric flexure and thermal anomalies, *J. Geophys. Res.*, 89, 11, 180–11, 194, 1984.
- McNutt, M. K., and H. W. Menard, Constraints on yield strength in the oceanic lithosphere derived from observations of flexure, *Geophys. J. R. Astron. Soc.*, 71, 363–394, 1982.
- Melosh, H. J., and C. A. Williams, Mechanics of graben formation in crustal rocks: A finite element analysis, *J. Geophys. Res.*, 94, 13, 961–13, 973, 1989.
- Moore, S. L., T. B. Thompson, and E. E. Foord, Structure and igneous rocks of the Ruidoso region, New Mexico, in *Geology of the Sierra Blanca, Sacramento and Capitan Ranges, New Mexico*, edited by J. M. Barker, B. S. Kues, G. S. Austin, and S. G. Lucas, *Field Conf. Guideb. N. M. Geol. Soc.*, 42, 137–145, 1991.
- Morgan, P., W. R. Seager, and M. P. Golombek, Cenozoic thermal, mechanical and tectonic evolution of the Rio Grande rift, *J. Geophys. Res.*, 91, 6263–6276, 1986.
- Mueller, S., and R. J. Phillips, On the reliability of lithospheric constraints derived from models of outer-rise flexure, *Geophys. J. Int.*, 123, 887–902, 1995.
- Nadai, A., *Theory of Flow and Fracture of Solids*, vol. 2, 348 pp., McGraw–Hill, New York, 1963.
- Olsen, K. H., W. S. Baldrige, and J. F. Callender, Rio Grande rift: An overview, *Tectonophysics*, 143, 119–139, 1987.
- Parker, E. C., P. M. Davis, J. R. Evans, H. M. Iyer, and K. H. Olsen, Upwarp of anomalous asthenosphere beneath the Rio Grande rift, *Nature*, 312, 354–356, 1984.
- Polyak, V. J., W. C. McIntosh, N. Güver, and P. Provencio, Age and origin of Carlsbad Cavern and related caves from $^{40}\text{Ar}/^{39}\text{Ar}$ of alunite, *Science*, 279, 1919–1922, 1998.
- Pray, L. C., Geology of the Sacramento Mountains escarpment, Otero County, New Mexico, *Bull.*, 35, 144 pp., N. M. Bur. Mines Min. Resour., Socorro, 1961.
- Reiter, M., R. E. Eggleston, B. R. Broadwell, and J. Minier, Estimates of terrestrial heat flow from deep petroleum tests along the Rio Grande rift in central and southern New Mexico, *J. Geophys. Res.*, 91, 6225–6245, 1986.
- Roberts, D. G., D. C. Adams, and G. R. Keller, A geophysical analysis of crustal structure in the Ruidoso area, in *Geology of the Sierra Blanca, Sacramento and Capitan Ranges, New Mexico*, edited by J. M. Barker, B. S. Kues, G. S. Austin, and S. G. Lucas, *Field Conf. Guideb. N. M. Geol. Soc.*, 42, 191–197, 1991.
- Russell, L. R., and S. Snelson, Structure and tectonics of the Albuquerque Basin segment of the Rio Grande rift: Insights from reflection seismic data, in *Basins of the Rio Grande Rift. Structure, Stratigraphy, and Tectonic Setting*, edited by G. R. Keller and S. M. Cather, *Spec. Pap. Geol. Soc. Am.*, 291, 83–112, 1994.
- Slack, P. D., P. M. Davis, W. S. Baldrige, K. H. Olsen, A. Glahn, U. Achauer, and W. Spence, The upper mantle structure of the central Rio Grande rift region from teleseismic P and S wave travel time delays and attenuation, *J. Geophys. Res.*, 101, 16, 003–16, 023, 1996.
- Steckler, M. S., Uplift and extension at the Gulf of Suez: Indications of induced mantle convection, *Nature*, 317, 135–139, 1985.
- Stein, R. S., G. C. P. King, and J. B. Rundle, The growth of geological structures by repeated earthquakes, 2. Field examples of continental dip-slip faults, *J. Geophys. Res.*, 93, 13, 319–13, 331, 1988.
- Stern, T., and U. ten Brink, Flexural uplift of the Transantarctic Mountains, *J. Geophys. Res.*, 94, 10, 315–10, 330, 1989.
- Turcotte, D. L., and G. Schubert, *Geodynamics*, 450 pp., John Wiley, New York, 1982.
- Tweto, O., Laramide (late Cretaceous–early Tertiary) orogeny in the southern Rocky Mountains, in *Cenozoic History of the Southern Rocky Mountains*, edited by B. F. Curtis, *Mem. Geol. Soc. Am.*, 144, 1–44, 1975.
- Tweto, O., The Rio Grande rift system in Colorado, in *Rio Grande Rift: Tectonics and Magmatism*, edited by R. E. Riecker, pp. 33–56, AGU, Washington, D. C., 1979.
- Villemin, T., F. Alvarez, and J. Angelier, The Rhine-graben: Extension, subsidence and shoulder uplift, *Tectonophysics*, 128, 47–59, 1986.
- Walker, J. R., Geomorphic evolution of the Southern High Plains, *Bull.*, 35, 32 pp., Baylor Geol. Stud., Waco, Tex., 1978.
- Wallace, M. H., and H. J. Melosh, Buckling of a pervasively faulted lithosphere, *Pure Appl. Geophys.*, 142, 239–261, 1994.
- Wdowinski, S., and G. J. Axen, Isostatic rebound due to tectonic denudation: A viscous flow model of a layered lithosphere, *Tectonics*, 11, 303–315, 1992.
- Weissel, J. K., and G. D. Karner, Flexural uplift of rift flanks due to mechanical unloading of the lithosphere during extension, *J. Geophys. Res.*, 94, 13, 919–13, 950, 1989.
- Wessel, P., Thermal stresses and the bimodal distribution of elastic thickness estimates of the oceanic lithosphere, *J. Geophys. Res.*, 97, 14, 177–14, 193, 1992.
- Winkler, D. A., Vertebrate-bearing eolian unit from the Ogallala Group (Miocene) in northwestern Texas, *Geology*, 15, 705–708, 1987.
- Woodward, L. A., J. F. Callender, J. Gries, W. R. Seager, C. E. Chapin, W. L. Shaffer, and R. E. Zilinski, Tectonic map of the Rio Grande region, Colorado–New Mexico border to Presidio, Texas, scale ~1:1,000,000, in *Guidebook of the Las Cruces Country*, edited by W. R. Seager, R. E. Clemons, and J. F. Callender, *Field Conf. Guideb. N. M. Geol. Soc.*, 26, 239, 1975.
- Zandt, G., and T. J. Owens, Crustal flexure associated with normal faulting and implications for seismicity along the Wasatch Front, Utah, *Bull. Seismol. Soc. Am.*, 70, 1501–1520, 1980.
- Zuber, M. T., and E. M. Parmentier, Lithospheric necking: A dynamic model for rift morphology, *Earth Planet. Sci. Lett.*, 77, 373–383, 1986.

C. D. Brown and R. J. Phillips, Department of Earth and Planetary Sciences, Washington University, Campus Box 1169, One Brookings Drive, Saint Louis, MO 63130-4899. (dbrown@geoid.wustl.edu)

(Received June 9, 1998;
revised May 12, 1999;
accepted May 27, 1999.)